Fault-controlled fluid circulation and diagenesis along basin bounding fault systems in rifts – insights from the East Greenland rift system

Eric Salomon[1,2], Atle Rotevatn[1], Thomas Berg Kristensen[1,3], Sten-Andreas Grundvåg[4], Gijs Allard Henstra[1,5], Anna Nele Meckler[1], Axel Gerdes[6], and Richard Albert[6]

[1]Department of Earth Science, University of Bergen, Bergen, Norway
[2]now at GeoZentrum Nordbayern, University of Erlangen-Nuremberg, Erlangen, Germany
[3]now at Equinor, Bergen, Norway
[4]Department of Geosciences, UiT The Arctic University of Norway, Tromsø, Norway
[5]now at AkerBP, Fornebu, Norway
[6]Department of Geosciences, Goethe University Frankfurt, Frankfurt, Germany

Correspondence: Eric Salomon (e.salomon@outlook.de)

Abstract. In marine rift basins, rift-climax deep-water clastics in the hanging wall of rift- or basin-bounding fault systems are commonly juxtaposed against crystalline basement rocks in the footwall. Displacing highly permeable, unconsolidated sediments against low-permeable rock distinguishes these faults significantly from others displacing hard rock. Due to limited surface exposure of such fault zones, studies elucidating their structure and evolution are rare. Consequently, their impact on

5   fluid circulation and in-fault, near-fault, and hanging wall sediment diagenesis are also poorly understood. Motivated by this, we here investigate a well-exposed strand of a major basin-bounding fault system in the East Greenland rift system, namely the Dombjerg Fault which bounds the Wollaston Forland Basin, NE Greenland. Here, Upper Jurassic and Lower Cretaceous syn-rift deep-water clastics are juxtaposed against Caledonian metamorphic basement.

Previously, a ~1 km-wide zone of increased calcite cementation of the hanging wall sediments along the Dombjerg fault core

10   was identified (Kristensen et al., 2016). Now, based on U-Pb calcite dating, we are able to show that cementation and formation of this zone started during the rift climax in Berrisian/Valanginian times. Using clumped isotope analysis, we determined a cement formation temperature of ~30–70°C. Temperatures likely do not relate to the normal geothermal gradient, but to elevated fluid temperatures of upward directed circulation along the fault.

Vein formation within the cementation zone clusters between ~125–100 Ma in the post-rift stage, indicating that fracturing in

15   the hanging wall is not directly related to the main phase of activity of the adjacent Dombjerg Fault. Vein formation temperatures are interpreted to reflect a shallow burial depth of the hanging wall deposits and range between ~30–80°C. Further, similar minor element concentrations of veins and adjacent cements argue for diffusional mass transfer into fractures, which in turn infers a subdued fluid circulation and low permeability of the fracture network. These results imply that the cementation zone formed a near-impermeable barrier quickly after sediment deposition and maintained this state even after fracture formation.

20   We argue, that the existence of such a cementation zone should be considered in any assessments that target basin-bounding fault systems for, e.g., hydrocarbon, groundwater, geothermal energy, and carbon storage exploration. Our study highlights that

the understanding of fluid flow properties as well as fault-controlled diagenesis affecting the fault itself and/or adjacent basinal clastics is of great fundamental and economic importance.

1 Introduction

During rifting and continental breakup, the rift border fault systems that develop may reach lengths of more than hundred kilometers, and accumulate vertical displacements of several kilometers (e.g., Morley, 1995; Ebinger et al., 1999; Whipp et al., 2014). Such fault systems, often guided by pre-existing basement structure (e.g., Ring, 1994; Corti et al., 2007; Salomon et al., 2015; Phillips et al., 2016; Rotevatn et al., 2018), generally exert strong controls on rift geometry, basin physiography, accommodation, and routing of syn-rift sedimentary systems (e.g., Gawthorpe et al., 1994; Sharp et al., 2000). A main character of these fault zones is their significant displacement of clastic syn-rift sediments against crystalline basement rock (e.g., Gawthorpe and Leeder, 2000).

Lithology plays an important part in the evolution of fault systems, especially in concert with fluid flow (Indrevær et al., 2014). The interaction between lithology, deformation, and fluid flow has attracted numerous studies since the proposition of the seismic pumping mechanism where seismic faulting triggers hydrothermal fluid injection through the fault core (Sibson et al., 1975). Research covers fault zones hosted by igneous (e.g., Mitchell and Faulkner, 2012), metamorphic (e.g., Wibberley and Shimamoto, 2003), carbonate (e.g., Smeraglia et al., 2016), mature sedimentary rocks or uncemented sediments (e.g., Pei et al., 2015, and references therein; Williams et al., 2015; Hollis et al., 2017). It has been shown that faults may serve as significant conduits (Hollis et al., 2017) or as baffles to fluid circulation (Rawling et al., 2001; Pei et al., 2015). Further, faults may comprise an initial high permeability due to intense fracturing and later become impermeable in consequence of veining (Cox, 1995). At the same time, the fault core may experience a different or even a contrasting permeability evolution than the damage zone surrounding the fault core (Sheldon and Micklethwaite, 2007; Indrevær et al., 2014).

Studies on syn-rift border faults displacing crystalline and/or metamorphic rocks against clastic sediments have contributed to a lesser degree to the understanding of the interaction of faults and fluids, which may primarily root in the limited exposure of such fault zones (e.g., Hollinsworth et al., 2019, and Kristensen et al., 2016, being notable exceptions). In such settings, there is a significant permeability contrast from footwall to hanging wall: the crystalline- / metamorphic footwall is commonly near-impermeable, while the unconsolidated sediments in the hanging wall are highly porous and permeable. Therefore, whereas fluid circulation mainly occurs in fractures in the crystalline "basement" footwall, large fluid volumes can potentially circulate through the pore space in the clastic hanging wall strata.

At the Dombjerg Fault in NE Greenland (Fig. 1), Kristensen et al. (2016) showed that a ∼1 km-wide envelope of calcite cement (termed "chemical alteration zone") formed in the hanging wall along the fault, which strongly argues for a significant influence of the fault on diagenesis of the adjacent sediments. This is an important observation, as the calcite cementation transforms the sediments from an unconsolidated to a consolidated state. This in turn changes the mechanical properties of the hanging wall rock, and affects how later deformation is accommodated: while deformation bands would form in the damage

55 zone within porous, non-cemented clastics, fractures form in low- to non-porous cemented clastics. It also significantly affects the permeability of the hanging wall clastics: where porous and non-cemented, fluids flow through open pore space and with flow being hampered only by deformation bands; however, where the clastics have low- to no porosity due to cementation, fluid flow becomes increasingly dependent on open fractures in an otherwise impermeable cemented sedimentary rock.

Hence, the identification of such a zone of enhanced cementation has important implications for the evaluation of near-fault
60 diagenesis and for the understanding of the linked deformational, diagenetic and fluid flow history of a fault zone. The fact that near-fault diagenesis significantly impacts flow properties, makes it economically significant, and highly relevant in, e.g., the exploration and exploitation of groundwater, hydrocarbon and geothermal resources, and for subsurface carbon storage sites. However, at present, fault seal analyses in reservoirs mostly rely on juxtaposition seals and shale smear, neglecting the effect of a cementation zone (e.g., Sperrevik et al., 2002; Yielding et al., 2010; Karolytė et al., 2020).

65 In this contribution, we aim to further elucidate the formation of cementation zones along syn-rift border faults. To do this, and building on Kristensen et al. (2016), we here investigate the evolution of the well-exposed cementation zone of the Dombjerg Fault in the Wollaston Forland of NE Greenland, where we combine the analysis of i) field and microstructural observations, ii) cement and vein formation temperatures based on clumped isotope analysis, iii) cement and vein formation ages based on U-Pb calcite dating, as well as iv) minor element compositions of cements and veins based on electron microprobe analysis.
70 We demonstrate that the cemented envelope formed soon after the deposition of rift-climax sediments at shallow burial depths, with vein formation occurring predominantly in the post-rift stage. We also show that even after fracturing, the cemented envelope formed an effective seal. The results offer a unique insight into near-fault diagenesis associated with major basin-bounding fault systems in rifts, showcasing the interplay of tectonic and diagenetic processes.

2 Geological Setting

75 The study area is located in the Wollaston Forland in NE Greenland and forms part of the East Greenland Rift System (Fig. 1). This rift system has experienced a long-lived extensional history since the late Paleozoic that eventually resulted in the opening of the North Atlantic in the Paleocene–Eocene (e.g., Larsen and Watt, 1985; Surlyk, 1990; Stemmerik et al., 1991). Onshore, the East Greenland Rift System is exposed along ∼600 km where a major right-stepping rift-bounding fault system displaces Permian to Cretaceous syn-rift sedimentary rocks against Caledonian metamorphic and crystalline basement (Fig. 1a). In the
80 Wollaston Forland, this rift-border fault system is marked by the ∼25 km long Dombjerg Fault with an approximately 3 km vertical throw (Fig. 1b,c; Surlyk and Korstgård, 2013). Activity of the Dombjerg Fault presumably started in the Mississippian and the fault was repeatedly active prior to the onset of the main rift phase in the Middle Jurassic (Rotevatn et al., 2018). To the North, the fault connects with the Thomsenland Fault through a ∼10 km-wide transfer zone.

The footwall block west of the Dombjerg Fault (referred to as the Clavering Block; Fig. 1c) comprises Caledonian migmatite
85 gneisses, pegmatites, amphibolites, felsic gneisses, mafic and ultramafic rock (Surlyk, 1978; Kristensen et al., 2016). East of the fault in the Wollaston Forland, the earliest sediments deposited, though not directly exposed along the fault, are of Permian age and constitute dolomites, carbonates, and anhydrites (Fig. 1b; Surlyk et al., 1986; Surlyk and Korstgård, 2013). These de-

posits are overlain by early syn-rift marine sediments of the Middle to Upper Jurassic (Fig. 1b) and constitute mainly shallow marine sandstone (Pelion Formation), alternating thin mudstone and marine sandstone (Jakobsstigen Formation), and marine

90 heterolith and mudstone with sandstone turbidites (Bernbjerg Formation; Surlyk and Korstgård, 2013).

Exposed sedimentary rocks in the hanging wall (referred to as the Kuppel-Kuhn Block, Fig. 1c) of the Dombjerg Fault are of Late Jurassic to Early Cretaceous age (Tithonian – Hauterivian), and are mostly sandstones and conglomerates that stratigraphically belong to the up to 3 km-thick Wollaston Forland Group (e.g., Surlyk, 1984). The sediments derived from footwall erosion and were deposited by gravity flows in a fully submarine environment during the rift climax and late syn-rift phases

95 (e.g., Surlyk, 1978, 1984; Henstra et al., 2016). The Wollaston Forland Group is divided into the rift climax succession of the Lindemans Bugt Formation (mid Volgian–late Ryazanian, i.e. ∼148–147 Ma) and the late syn-rift succession assigned to the Palnatokes Bjerg Formation (latest Ryazanian–early Hauterivian; Surlyk, 1984; Surlyk and Korstgård, 2013; Henstra et al., 2016). This study only pertains to the rift-climax deposits of the Lindemans Bugt Formation.

The Lindemans Bugt Formation consists mainly of conglomerates and sandstones that form a clastic wedge bounded to the

100 west by the Dombjerg Fault, extending 10–15 km eastward into the basin before it gradually thins across the tilted crest of the hanging wall block (Fig. 1c). Close to the basin-bounding border fault, the hanging wall clastic succession is ∼2 km thick with strata dipping at 10–15° towards the basin axis to the east (Surlyk and Korstgård, 2013; Henstra et al., 2016). Further basin-ward, the thickness of the succession decreases and the inclination eases with strata being more sub-horizontal. On the adjacent dip-slope of the hanging wall block, the strata display gently dips up to 6° towards the basin axis to the west (Surlyk

105 and Korstgård, 2013; Henstra et al., 2016). Collectively, the thickness and dip variations reflect the asymmetric geometry of the basin, which is typical of basins developing from fault block rotation (e.g., Gawthorpe and Leeder, 2000). Thus, it is reasonable to assume that the basin was deepest close to the border fault, offering available accommodation for a thick succession of gravity flow deposits to accumulate (Surlyk, 1984; Henstra et al., 2016).

Within a ∼2 km-wide zone along the fault, the Lindemans Bugt Formation hosts up to several meters wide, brecciated clasts

110 consisting of metamorphic and crystalline basements rocks, and unsorted boulder to gravel-size conglomerate beds with average thicknesses exceeding 3 m. Some of the thicker conglomerate beds extend far into the basin (Henstra et al., 2016). Further basin-ward, amalgamated conglomerate–sandstone packages give way to normally graded, gravelly sandstone and sandstone beds with tabular geometries (Henstra et al., 2016). Normally-graded, fine-grained sandstone beds alternating with thin mudstone beds to form heterolithic sheet-like units (Henstra et al., 2016), typically occur in fault-distal locations, but locally also

115 occur intercalated with the coarse clastics in close proximity to the fault.

The Dombjerg Fault dips ∼65° to the ENE (Kristensen et al., 2016) and has an estimated maximum throw of ∼3 km to the base of the rift (Surlyk and Korstgård, 2013). Within a zone of ∼200 m width, located in basement rock, the fault consists of multiple fault core strands comprising fault gouge and intense brecciation (Kristensen et al., 2016). The footwall damage zone is ∼600 m wide comprising veins, fractures, and minor faults at increasing quantity towards the fault (i.e. from 4 joints and 1

120 vein per meter outside the damage zone to >50 joints and 20–30 veins per meter near the fault core; Kristensen et al., 2016). In the hanging wall, the sedimentary rock of the Lindemans Bugt Formation is characterized by intense calcite cementation extending approximately 1 km into the basin. Calcite veins cut through the cemented rock and are overprinted by joints. Their

quantity increases from zero joints and veins per meter outside the damage zone to 7 joints and veins per meter near the fault zone (Kristensen et al., 2016).

3 Methodology

This study is based on field analyses and samples taken during a 10-day field season in August 2018, supplemented with samples collected in an earlier field season in 2014. Outcrops were chosen by accessibility and were mostly confined to the hanging wall of the Dombjerg Fault as snow fields covered the footwall. Thin sections of samples were analyzed through optical microscopy, scanning electron and SEM cathodoluminescence microscopy on a Zeiss Supra 55VP, cold-cathode cathodoluminescence on a Technosyn 8200 Mk II, and Raman spectroscopy on a Horiba LabRAM HR. 30 thin sections of samples from the Lindemans Bugt Formation have been analyzed regarding their diagenetic character. 18 of these samples derive from the cementation zone, 3 samples from the carbonate-cemented lenses outside the cementation zone, and 9 samples from (carbonate-) uncemented sandstone (Fig. 2).

U-Pb analysis for calcite dating was performed at FIERCE (Frankfurt Isotope & Element Research Center), Goethe-University Frankfurt, with a RESOLution 193 nm ArF excimer laser (CompexPro 102) equipped with a two-volume ablation cell (Laurin Technic S155) coupled to a sector field ICP-MS (ElementXr, ThermoScientific). Before the analysis, the samples were screened, to find suitable areas for further analysis. This was successful on five calcite cement samples and 12 calcite vein samples, with a total of 25 vein growth phases, of the Lindemans Bugt Formation. Calcite vein samples of the basement and near the fault core did not provide appropriate U and Pb signals. Full details of the U-Pb analysis are described in the supplements. All uncertainties are reported at the 2σ level.

Clumped isotope analysis was conducted on 11 carbonate vein (10 calcite, 1 dolomite) and five calcite cement samples. In two calcite veins, two growth generations were analyzed (samples G-10 and G-36). Of the 11 vein samples, eight derive from the hanging wall sedimentary rock of the Lindemans Bugt Formation, two from brecciated basement rock close to the fault core, and one from basement rock in the transfer zone between the Dombjerg and Thomsenland Fault (Fig. 2). Hanging wall vein samples were chosen to spatially cover the cementation zone as best as possible. The selection of cement samples was guided by the feasibility of mechanically separating sufficient cement from the rock, which was successful on five samples. Four of these cement samples are from within the cementation zone and one (H-5) from an isolated cemented layer outside the chemical alteration zone.

Clumped isotope analysis was performed on a Thermo Fisher Scientific MAT-253 Plus isotope ration mass spectrometer coupled to a Thermo Fisher Scientific Kiel IV carbonate preparation device, where samples are reacted individually with phosphoric acid at 70°C. For each sample, 13–14 replicate measurements were performed, spread over 6 months. Results were pressure-baseline corrected (Bernasconi et al., 2013; Meckler et al., 2014) and transferred into the absolute reference frame (Dennis et al., 2011) using carbonate standards (ETH 1-3) measured alongside the samples, employing their accepted values determined by Bernasconi et al. (2018). All data processing was performed with the Easotope software (John and Bowen, 2016). For further details of the method, see Piasecki et al. (2019) or Meinicke et al. (2020). The clumped isotope analysis

also yields oxygen and carbon isotope values for each replicate, which have been corrected for drift using the same carbonate standards, with a two-point scale correction ("stretching") applied to $\delta^{18}O$ results.

Clumped isotope results (Δ_{47}) were averaged by sample and formation temperatures were calculated after Kele et al. (2015), using the updated version from Bernasconi et al. (2018), for calcite samples and after Müller et al. (2019) for dolomite samples.

160 For the calculation, we neglected replicates whose Δ_{47} value deviated from the sample average by 3x the standard deviation of the standards, which in total affected only one replicate. As clumped isotope temperatures are determined independently of fluid isotopic composition, the results can be used in combination with the measured oxygen isotopic values (carbonate $\delta^{18}O_{VPDB}$) to calculate fluid $\delta^{18}O_{VSMOW}$. For calcite samples, fluid $\delta^{18}O_{VSMOW}$ was calculated after Kim and O'Neil (1997, updated with fractionation factor of 1.01025), and for dolomite samples the calibration of Horita (2014) was used. All un-

165 certainties are presented at the 95 % confidence interval. The uncertainty for fluid $\delta^{18}O_{VSMOW}$ is given from the uncertainty propagation using the 95 % confidence intervals of the clumped isotope temperature and carbonate $\delta^{18}O_{VSMOW}$ and calculated as

$$\sqrt{\left(\frac{\partial fluid^{18}O}{\partial T} \cdot \Delta T\right)^2 + \left(\frac{\partial fluid^{18}O}{\partial carb^{18}O} \cdot \Delta carb^{18}O\right)^2} \tag{1}$$

Electron microprobe analysis for minor element concentrations (Mg, Fe, Mn, Sr) of calcite veins and cements was conducted

170 on a Cameca SX100 at accelerating voltage 15kV, beam current 10nA, counting time on peak 20s, and total counting time on background 20s. Detection limits were 300 ppm (Mg), 540 ppm (Fe), 630 ppm (Mn), and 420 ppm (Sr). For each analyzed vein generation 10 points were measured, and 20 points for cements as the latter has shown a larger variability in element concentrations.

4 Results

4.1 Cementation zone and diagenetic character of hanging wall sediments

The cementation zone forms an envelope of variable width along the Dombjerg Fault and we estimate its maximum width to be ∼1.5 km (Fig. 2), which is a bit larger than previously assessed (∼1 km; Kristensen et al., 2016). Within this zone, calcite cementation is prominently distributed and occurs in sedimentary layers of all grain sizes, while uncemented layers occur

180 occasionally and are usually less than 50 cm thick. At the fault-distal limit of the alteration zone, outcrops show cemented layers with "holes" formerly filled with now-eroded uncemented material (Fig. 3c). It appears that the cemented layers enclosed pockets of calcite-cement free sediments. Farther into the basin, calcite cement is absent in the vast majority of outcropping sediments (Fig. 3e) and only occurs occasionally as single isolated lenses in predominantly matrix-supported conglomerates. Calcite cement occurs as drusy spar (Fig. 4b) and in a coarse spar to poikilotopic texture (Fig. 4c). Drusy spar is present in 11

185 samples, all of which also comprise a varying amount of coarse calcite spar. Poikilotopic texture occurs in only two samples from within the cementation zone and in three samples from cemented lenses outside the cementation zone. Notably, sample

TBK2 hosting poikilotopic calcite derives from the same outcrop as sample TBK1 hosting drusy spar (Figs. 2, 4b,c). Biogenic calcite clasts are occasionally present in the cemented samples and show no signs of dissolution or recrystallization. Feldspar overgrowth occurs in both cemented and uncemented samples (Figs. 4d,f), but is commonly more pronounced in the

190 latter sample suit. Feldspar grain dissolution is absent or only occurs to a minor degree in uncemented samples. The calcite-cemented samples comprise minor to major feldspar dissolution (Figs. 4b,c), although complete grain dissolution does not occur. Quartz overgrowth has not been detected in the samples. Quartz grain dissolution is only a minor component in cemented samples and absent in uncemented samples (Fig. 4).

195 **4.2 Vein structure and composition**

In all outcrops within the cementation zone, calcite veins were found (Fig. 3b), which have an overall NNE to NE trend (67 veins measured in total; Fig. 2). Outcrop surfaces were exposed in 3-D and we hence conclude that this dominant vein trend is true and not biased by outcrop orientation. Veins exclusively occur in cemented parts of the hosting sandstone and single vein thicknesses span from <1–70 mm. Two thirds of the analyzed veins comprise two or more vein growth generations, indicated

200 by either crack-seal texture (i.e. precipitation after reopening of fracture) or growth zonation (Figs. 5a,b).

Near the fault core within brecciated basement rock, two vein generations were identified: a dolomite vein network that is cross-cut by a younger calcite vein network (Fig. 3a). The dolomite network is prominently visible and composes of continuous, anastomosing veins of varying thicknesses up to 30 mm (Figs. 3a, 5e). The younger calcite vein network consists of planar veins with thicknesses of ∼1–5 mm (Fig. 3a) and fills voids within the dolomite veins as well (Fig. 5f). As far as visible, the

205 dolomite veins are not displaced/offset by the calcite veins and the latter are as well not displaced by any other fracture set. In the transfer zone, connecting the Dombjerg and Thomsenland faults (Fig. 2), only one calcite vein was found in a shear fracture that reactivated an older epidote vein.

4.3 Ages of calcite cements and veins

210 We determined formation ages of five cement samples and 12 vein samples within the sediments of the Lindemans Bugt Formation (Table 1, fig. 6). As some veins comprise more than one growth generation, as evident by zoning or fracture re-opening, we obtained a total of 25 growth ages of the 12 vein samples. Age determination of veins within the basement and fault core were not successful due to unsuitable U and Pb signals.

Three cement ages fall within the previously reported depositional age of the Lindemans Bugt Formation or close to its depo-

215 sitional age boundary with the Palnatokes Bjerg Formation with 150.6 ± 9.3 Ma (G-36cem), 143.7 ± 6.5 Ma (TBK1cem), and 139.4 ± 4.9 Ma (G-38cem). The two other cement ages are significantly younger with 103.3 ± 2.6 Ma (TBK2cem) and 102.9 ± 3.7 Ma (G-9cem) and most likely reflect calcite recrystallization ages (see discussion chapter 5.1). Of the vein samples, only one falls within the inferred rift stage with 139.3 ± 3.4 Ma (G-10 v1), while the majority of vein ages (both initial formation ages and vein reopening ages) fall within a range of ∼125–90 Ma (Fig. 6). Two vein ages are significantly younger with $50.1 \pm$

220 2.1 Ma (G-7) and 49.4 ± 2.1 Ma (G-2), closely post-dating early Eocene plateau basalt extrusion and the onset of continental breakup (Fig. 6).

4.4 Clumped isotope temperatures of calcite cements and veins

Clumped isotope temperatures of five calcite cement samples were obtained. Temperatures from TBK1cem and the recrystal-

225 lized TBK2cem, which derive from the same outcrop, are 42.0 ± 10.2˚C and 59.0 ± 9.1˚C, respectively. G-25cem, sampled at a similar distance to the main fault core, has a clumped isotope temperature of 42.4 ± 8.8˚C, G-36cem at the distal margin of the cementation zone has 56.6 ± 10.9˚C, and H-5cem, located well into the basin, has 44.5 ± 9.0˚C (Table 2, Fig. 2).

Clumped isotope temperatures of hanging wall veins fall into the range of 36.3 ± 9.4˚C (G-36 v1) and 77.6 ± 10.1˚C (G-22). In the two samples of which two vein generations were analyzed, a temperature increase exists from old to young vein phase

230 (i.e. G-36 from 36.3 ± 9.4˚C to 58.2 ± 14.1˚C and G-10 from 40.3 ± 7.1˚C to 61.5 ± 10.5˚C; Table 2, fig. 5a). However, taking all samples, including cement samples, into consideration, no clear trend in temperature evolution with time is visible (Fig. 7a), which is also true for the relationship of temperature and distance to the fault core (Fig. 7b). The clumped isotope temperature of the basement vein sample G-34 yields 128.7 ± 19.1˚C. Near the fault core in brecciated basement, the clumped isotope temperature of the younger calcite vein (TBK9cal) falls with 68.8 ± 10.9˚C into the range of hanging wall vein temperatures.

235 The older dolomite vein sample TBK9dol diverges from this pattern with a higher temperature of 106.5 ± 11.9˚C (Fig. 5f; Table 2).

4.5 Minor element concentrations of cements and veins

For the minor element concentration analysis, we studied 10 calcite cement samples, 12 hanging wall calcite vein samples, two

240 samples of veins from the fault core (one dolomite, one calcite vein), and one basement calcite vein sample (Table 3, Fig. 8). As some hanging wall samples comprised multiple vein growth generations, we measured in total 22 growth generations in the 12 hanging wall samples.

Common to all samples is a Sr concentration below or close to the detection limit and will therefore be neglected in the follow-ing. Cements comprise element concentration averages of 2429–11862 ppm (Fe), 2866–5045 ppm (Mn), and 1152–7557 ppm

245 (Mg) (Table 3). Hanging wall veins yield similar averages with values of 1436–13598 ppm (Fe), 2515–6719 ppm (Mn), and 401–5180 ppm (Mg). The two Eocene-aged hanging wall veins G-2 and G-7 differ significant with Fe and Mg concentrations being below the detection limit, and Mn concentration below detection in sample G-2, and 2390 ppm in sample G-7. The same accounts for the basement sample G-34 with Fe, Mn, and Mg concentrations being below the detection limit. The fault core vein TBK9cal yields concentrations of 8342 ppm (Fe), 1435 ppm (Mn), and 887 ppm (Mg). Naturally, the older fault core

250 dolomite vein TBK9dol diverges from the other samples with a high Mg and Fe concentration of 112599 ppm and 24556 ppm, respectively, and a low Mn concentration of 1219 ppm.

The comparison of veins and respective cements from the immediate wall rock within a sample shows similar Mg- and Mn-

concentrations for a majority of samples (i.e. samples G-4, G-9, G-22, G-25, and G-38; Fig. 8), which also partly accounts for Fe (G-4, G-25, G-38; Fig. 8). Overall, the Fe/Mn/Mg ratio is similar from cement to vein within half of the samples, whereas

255 concentration and ratios differ from sample to sample (e.g., compare G-25 and G-38; Fig. 8). Vein generations within a sample do not show significant variations in minor element concentrations (supplementary figure S2). No trends in concentration or ratio versus time or spatial distribution are evident.

5 Discussion

260 ### 5.1 Timing and formation environment of the cementation zone

Based on the U/Pb calcite cement ages of 150.6 ± 9.3 Ma, 143.7 ± 6.5 Ma, and 139.4 ± 4.9 Ma (samples G-36, TBK1, G-38), the formation of the cementation zone in the hanging wall has likely occurred during or immediately after the deposition of the hosting sediments of the Lindemans Bugt Formation during the rift climax (Fig. 6). The 150.6 Ma age of G-36 is unrealistic as it predates the Lindemans Bugt Formation, however its error margin reaches well into the time interval over which this

265 formation was deposited (Fig. 6; e.g., Surlyk, 2003).

The two younger cement ages of 104.1 ± 1.7 Ma (G-9cem) and 103.3 ± 2.6 Ma (TBK2) do not reflect a second cement growth phase, but are recrystallization ages, for the following reasons: In sample G-9, one vein generation is with 115.5 ± 3.1 Ma (G-9 v4) significantly older than the cement age. Based on this, it is plausible that the wall rock was cemented before ~115.5 Ma to provide the tensile strength for the discrete fracture to form. In sample TBK2, deriving from the same outcrop

270 as TBK1, the cement has a well-developed coarse sparitic to poikilotopic texture (Fig. 4c) with crystal sizes that exceed any other analyzed cement sample. This type of texture has also elsewhere been interpreted as evidence for recrystallization (e.g., Saigal and Bjørlykke, 1987; McBride and Milliken, 2006; Worden et al., 2019).

A second argument for a cementation zone formation during or immediately after deposition is the age of vein G-10 v1 with 139.3 ± 3.4 Ma, which is close to the upper boundary (age-wise) of the Lindemans Bugt Formation. deposition. In line with

275 our argument based on sample G-9 above, it is unlikely that fractures would form unless the formation was already at least partly cemented.

Having established that the cementation zone formed immediately after deposition of the Lindemans Bugt Formation, its maximum formation depth is constrained by the thickness of the remaining part of the unit above the sampled intervals. The litostratigraphic top of the Lindemans Bugt Formation is exposed on a ridge ~4500 m away from the Dombjerg Fault (Fig.

280 2). Using a maximum depositional dip angle of 15° for fault-proximal Lindemans Bugt Formation sedimentary strata (Henstra et al., 2016) allows to interpolate the top of this formation towards the fault (Fig. 9). With this approach, we estimate a maximum thickness of the Lindemans Bugt Formation above sample TBK1cem of ~1050 m and above sample G-36cem of ~750 m. These thicknesses represent maximum estimates, because the depositional slope angle of the sediments decreases away from the fault. Applying an angle of 10° would for example lower the estimated thickness to 740 m and 530 m above

285 samples TBK1cem and G-36cem, respectively (Fig. 9). Hence, we can confidently estimate that the cementation zone formed

at a burial depth of ∼1000 m or less (compaction not accounted for).

Formation temperatures of the cements can be assessed from the clumped isotope temperatures, although their interpretation needs to be taken with care: Calcite is subject to solid-state reordering of C-O bonds at ambient temperatures > ∼100°C, which affects the Δ_{47} composition and subsequently deviates the clumped isotope temperature from the initial formation temperature
290 (Passey and Henkes, 2012). For dolomite, solid-state reordering starts at ambient temperatures of ∼150°C (Lloyd et al., 2018). It is documented that this resetting is a challenge especially for samples from sedimentary basins, where the rock may have experienced high burial temperatures for long time periods (Henkes et al., 2014; Shenton et al., 2015). For the sedimentary rock of the Lindemans Bugt Formation, the absence of quartz overgrowth in both calcite-cemented and uncemented sediment samples provides a control on the maximum burial temperature. Temperature is a critical factor on the formation of quartz
295 cement, which is known to start at ∼70°C and its growth rate increases significantly with increasing temperature (e.g., Walderhaug, 1994; Lander and Walderhaug, 1999; Harwood et al., 2013). Therefore, we argue that the analyzed samples from the Lindemans Bugt Formation have not been subject to temperatures above 100°C and that the clumped isotope temperatures reflect the formation temperatures. However, this excludes samples that were subject to recrystallization, i.e. dissolution and reprecipitation (Eiler, 2011), as well as the basement and fault core samples, whose age/temperature history is not known.
300 Formation temperatures of cements are relatively high when considering their shallow formation depth, e.g. 56.6 ± 10.9°C for G-36cem and 42.0 ± 10.2°C for TBK1cem. For example, for sample G-36cem, given its formation temperature, a formation depth of 530-750 m (Fig. 9), and an assumed near-surface groundwater temperature of 10°C, a geothermal gradient of 73 ± 21°C/km can be calculated, which argues for upward flow of hot fluids along the fault. Localized high geothermal gradients near faults are common and have been reported along other fault systems, such as at the western Svalbard margin (Vanneste
305 et al., 2005), in southern Tuscany/Italy (Bellani et al., 2004), and along the Southern Alpine Fault Zone in New Zealand (Townend et al., 2017). The temperature difference between samples G-36cem (56.6 ± 10.9°C) and TBK1cem (42.0 ± 10.1°C), despite being similar in age, indicates that fluid circulation and temperature distribution did not occur homogeneously in the hanging wall samples, and that highest temperatures are not necessarily found closest to the fault. This may root in permeability variations within the hanging wall deposits, due to e.g. grain size, sorting, or onset of cementation, which may cause local
310 perturbation or channeling of fluid flow and advective heat transfer.

The fluid $\delta^{18}O_{VSMOW}$ values of the cements likely reflect a marine or potentially a mixed meteoric/marine fluid system, which is unsurprising given the marine deposition environment in the hanging wall basin. The values appear to increase slightly with distance to the fault (Fig. 7c) and with the caveat that this observation is based on a limited number of data points, this may be taken to suggest that an influx of meteoric groundwater affected the proximal (near-fault) parts of the hanging wall but did not
315 access the more proximal hanging wall deposits.

5.2 Timing and formation of calcite veins

The analyzed veins cover a U-Pb age range from 140 to 90 Ma. Only one of these veins (sample G-10 v1) formed during the rift climax stage (Table 1, fig. 6), whereas the majority formed broadly between 125 to 100 Ma in the post-rift stage, accompanied

320   by renewed fracture opening and vein formation between 115 to 90 Ma (Fig. 6). Extensional phases have not been reported for the Wollaston Forland during the Aptian to Turonian. However, on northern Hold with Hope, ∼80 km south of our study area (Fig. 1), a rift period occurred from end-Valanginian to Middle Albian times with faulting along a series of N–NNE trending normal faults (Whitham et al., 1999). Both vein ages and orientations in our study area fit well with these structures and might therefore correspond to this tectonic phase. On the rift counter-part across the Norway-Greenland Sea, the Lofoten-Vesterålen

325   segment of the Norwegian continental shelf, a rifting phase occurred during the Late Albian (Dalland, 1981; Henstra et al., 2017) and may have a minor contribution to fracturing or fracture reopening.

It is also possible that the veins formed in two stages by i) fracturing during the main rift stage, and ii) fracture cementation in the post-rift stage. However, the vein generation G-10 v1 precipitated at the end of the rift climax (Fig. 6; table 1) showing that the formation conditions were favorable for calcite precipitation. Hence, it would be reasonable to expect that also other

330   fractures forming during rift climax should be cement-filled, and we therefore consider the above two-stage interpretation as less likely, and our preferred interpretation is that the veins formed in their entirety in the post-rift stage. The U-Pb ages of vein samples G-7 (50.1 ± 2.1 Ma) and G-2 (49.4 ± 2.1 Ma) diverge significantly from the main sample suit. These veins closely post-date the extrusion of the plateau basalts covering the Lower Cretaceous late syn-rift Palnatokes Bjerg Formation. This event is dated to 56-53 Ma (Larsen et al., 2014) and is related to the onset of continental breakup, which started at the latitude

335   of the Wollaston Forland around 55 Ma (Mjelde et al., 2008; Larsen et al., 2014). Hence, the formation of the veins could be directly related to deformation and uplift following breakup. A second striking difference to the main sample suit is the fluid $\delta^{18}O_{VSMOW}$ value available for G-7, which with -13.7 ± 1.5 clearly indicates a meteoric fluid. We therefore interpret that deformation and, potential, rift shoulder uplift in response to continental breakup (e.g., Wernicke, 1985; Chéry et al., 1992), was responsible for vein formation, which at this time occurred under meteoric conditions.

340   As outlined in the previous chapter, the clumped isotope temperatures of the hanging wall veins most likely reflect their formation temperatures. These generally lie close to the cement formation temperatures, which may be explained by i) similar formation depth, ii) deeper formation depth, but lower geothermal gradient, or iii) perturbation of fluid flow and advective heat transfer. The latter argument should be valid as the cementation zone has likely created a setting for complex fluid pathways. While the evolution of the geothermal gradient is difficult to assess, the burial depth of the analyzed sedimentary rock has

345   increased due to continued deposition of sediments in the hanging wall basin in the late syn-rift and post-rift stage (e.g., Surlyk and Korstgård, 2013). Two formation temperatures and ages are obtained of successive precipitation generations from two vein samples, respectively (samples G-10 and G-36; Table 2, fig. 5a). Both samples yield an increase of formation temperature from old to young (i.e. from 40.3 ± 7.1°C to 61.5 ± 10.5°C in sample G-10 and from 36.3 ± 9.4°C to 58.2 ± 14.1°C in sample G-36), which might indeed reflect an increasing formation depth. However, the possibility persists that the connectivity of fluid

350   pathways may have been in a favorable condition for warmer fluids to circulate through the fractures during the formation of the younger vein generations.

For the calcite and dolomite samples from the basement and fault core, it is unclear if the clumped isotope temperatures reflect the original formation temperatures, since an age control is missing. Therefore, these samples may have been partially reset due to ambient temperatures above the threshold of C-O bond reordering of ∼100°C for calcite (Passey and Henkes, 2012)

355 and ∼150°C for dolomite (Lloyd et al., 2018) in the course of time. For the basement sample G-34, with a clumped isotope temperature of 128.7 ± 19.1°C, this possibility may have resulted in a complex mixed signal of original formation, maximum, and cooling temperatures. For the fault core vein samples, only a partial heating signal may be present as the measured clumped isotope temperatures of both veins are still below the temperature threshold (i.e. a fully reset signal would give a clumped isotope temperature above 100°C for calcite and 150°C for dolomite). Therefore, we are confident that the original

360 formation temperatures of the dolomite and calcite vein samples from the fault core are ≤106.5 ± 11.9°C and ≤68.8 ± 10.9°C, respectively. Since both vein networks have a continuous, non-faulted appearance (Fig. 3a), we argue that these veins formed in the late stage of fault activity.

5.3 Origin of calcite components and fluid circulation patters

365 One of the main questions around the formation of the cementation zone is the origin of calcium necessary for the calcite cementation. A first likely candidate for a source is calcium from seawater that circulated through the hanging wall clastics (Morad, 1998). Such a circulation may be expected to follow general subsurface flow patterns in coastal areas. In such areas, groundwater systems are commonly characterized by saline (i.e. seawater) groundwater circulation that is tidal-, density-, and thermal-driven, and meteoric groundwater flow towards the ocean, driven by the hydraulic head (e.g., Cooper, 1959; Wilson,

370 2005; Jiao and Post, 2019). Permitted the presence of a continuous and undisturbed permeable rock, saline circulation is not restricted to the aquifer underneath the ocean, but extends landward beyond the coastline underneath the body of meteoric groundwater (Fig. 10a). The landward extension of saline groundwater circulation partly depends on the permeability of the aquifer (e.g., Houben et al., 2018; Jiao and Post, 2019). Along the Dombjerg Fault, which defined and delineated the coastline during the rift climax, the footwall is composed of low-permeable crystalline and metamorphic rock with a low fracture and

375 vein density (4 joints + 1 vein per meter; Kristensen et al., 2016). On the other hand, the hanging wall clastics have distinctly different flow properties than that of low-permeable crystalline basement. Where non-cemented, these deposits are highly permeable allowing for fluid flux at a much larger degree compared to low-fractured crystalline and metamorphic basement rock (e.g., Brace, 1980). Hence, along the Dombjerg Fault, saline fluid circulation should be predominantly restricted to the permeable fault zone and hanging wall clastics (Fig. 10b). Upwelling of warm saline fluids within the clastics along the fault may

380 have been in a favorable condition for the precipitation of calcite from seawater.

A second candidate for a calcium source are Permian carbonate and evaporite deposits underlying the clastic hanging wall rift sediments. While a direct exposure of such rock along the Dombjerg Fault is missing, a Permian carbonate unit is located along the northern section of the Clavering Fault (Fig. 1b; Surlyk, 1978), which forms the southern extension of the Dombjerg Fault. Permian carbonate rock is also exposed at the southern crest of the hanging wall block of the Dombjerg Fault (Fig. 1b;

385 Surlyk, 1978). It may therefore be a reasonable assumption that the Permian succession is also underlying the Lindemans Bugt Formation along the Dombjerg Fault, especially considering that the fault had been active since the Carboniferous (Rotevatn et al., 2018). It has been proposed and modeled elsewhere that surface waters may convect thermally-driven within faults (e.g., López and Smith, 1996; Zhao et al., 2003; Hollis et al., 2017). Such convecting fluids within the Dombjerg Fault may have

dissolved the carbonate and transported the solutes into the Lindemans Bugt Formation for the precipitation of calcite.

390   Other potential sources for calcium can be excluded: No carbonate rock is hosted by the basement and also carbonate deposits in the Palnatokes Bjerg Formation overlying the cementation zone-hosting Lindemans Bugt Formation (i.e. Albrecht Bugt Member; Surlyk and Korstgård, 2013) can be ruled out as a source, since the cementation pre-dates this deposition. Further, dissolution of biogenic carbonate clasts and feldspar alteration appear unlikely for a potential internal source. Although biogenic carbonate clasts occur sporadically in some outcrop sections and are visible in a number of thin sections, they do not

395   show signs of dissolution or recrystallization. The degree of feldspar alteration in the sandstone is low and, hence, will not have provided a significant amount of calcium. Therefore, whether calcium from seawater or dissolved underlying carbonates, it is clear that the calcium must have been introduced into the sediments of the Lindemans Bugt Formation by advective transfer. CO_2 that is acquired for the formation of calcite may have been generated and transported along in the same process. Yet, the negative $\delta^{13}C_{VPDB}$ values of the cements hint towards an (additional) internal source: $\delta^{13}C$ values of calcite cements range

400   from -18.2 to -9.7, which are typical values for CO_2 deriving from the degradation of organic matter (e.g., Clark and Fritz, 1997). The high Uranium content of the cements, which allowed the U-Pb calcite dating, also argues for degradation of organic matter, which is commonly bonding Uranium (e.g., Spirakis, 1996; Cumberland et al., 2016).

5.4   Permeability of the fault and the cementation zone

405   Throughout its seismic activity, the Dombjerg Fault was permeable due to repeated fracturing, as commonly assigned to fault zones (e.g., Sibson, 1990). The anastomosing dolomite vein network (represented by sample TBK9dol) close to the fault core suggests the fault represented a conduit for vertical (up-fault) fluid migration. It yields a fluid $\delta^{18}O$ value of $+16.1 \pm 1.6$ (Table 2), which is by far the highest value determined in our sample suit and is indicative for a metamorphic fluid (Sheppard, 1986) that was likely sourced from greater depths. On the contrary, its formation temperature of $\leq 106.5 \pm 11.9$°C is not particularly

410   high, which might reflect a moderate flow rate allowing the fluid to adapt to the ambient wall rock temperature.
The younger calcite vein network cutting through the dolomite veins is less pronounced and consists of thinner veins. Its fluid $\delta^{18}O$ value of -1.8 ± 1.7 (sample TBK9cal; Table 2) indicates a marine fluid, which may be taken to suggest that the saline groundwater circulation was responsible for its formation. The $\delta^{13}C$ value of -4.2 ± 0.1 of this vein differs significantly from hanging wall cements and veins (-23.5 to -9.7). Also, the minor element concentration ratio diverges from hanging wall samples

415   (Table 3, Fig. 8). This might indicate that the saline groundwater circulation, from which the calcite in the fault core fracture network precipitated, was decoupled from groundwater circulation in the hanging wall sediments.
In the hanging wall, the cementation zone will have, once formed, significantly lowered the permeability of the fault-proximal hanging wall sediments, as the carbonate cement reduces the pore space towards 0 %. During progressive formation of the cementation zone and accompanying matrix porosity and permeability loss, fluid circulation becomes increasingly dependent

420   on flowing through fractures developed within this zone. Here, the magnitude of circulation and flow direction is then guided by the connectivity and orientation of the fracture network.
A hint towards the degree of fracture connectivity and fluid flow rate is given by the minor element concentration of cements

and veins (Fig. 8). There is a striking similarity of minor element concentrations between veins and the respective wall rock cement in around half of the analyzed samples. As this pattern is visible in both sample suits of original and recrystallized cement, this pattern seems to be a primary signal, i.e. reflecting the fluid composition of the initial calcite formation. Hence, the solute which formed the vein calcite likely derived from diffusion from the calcite cement into the fracture. It should be noted, that the possibility of a later equilibrium between cements and vein through solid state diffusion cannot be fully neglected, as this is a process that is poorly understood at low temperatures, though experiments point towards an unlikely mechanism (Fisler and Cygan, 1999; Gorski and Fantle, 2017).

430 If true, i.e. diffusion being responsible for the vein calcite formation, this indicates very slow advective fluid circulation and a poorly connected fracture network. As the veins are predominantly parallel with a NNE-strike and near-vertical dip, an interconnection between these veins might have indeed been poor. This emphasizes that the cementation zone was nearly impermeable despite having been subject to fracturing.

6 Summary and Conclusions

The integration of the analyses of our sample suits sheds light on the fluid flow evolution along the Dombjerg Fault since its syn- to late-rift stage activity. Within the fault, a well-connected fracture network existed at the late stage of fault activity allowing upward flow of metamorphic fluids (Fig. 11a), as evident by the dolomite vein network. At depth, these fluids may have been dragged into the highly fractured fault, where thermal-driven upward flow occurred. Presumably, such networks existed repeatedly in the course of the faults activity. Towards the end of its activity, the fault became sealed to deep fluid circulation, as indicated by the less-pronounced, low-temperature calcite vein network postdating the prominent dolomite vein network.

In the hanging wall, fluid advection followed the common model of groundwater flow in coastal aquifers, with the distinction that thermal-driven upward flow occurred within the sediments along the fault and low-permeable footwall rock (Fig. 10, 11). The cementation zone formed quickly after the deposition of its hosting sediments of the Lindemans Bugt Formation (Fig. 11b), with a formation temperature around 30–70°C at a depth <1 km (Fig. 9). While the calcium for the calcite formation derived from advective fluid transport, CO_2 likely has a component of local formation. Once formed, the cementation zone acts as a low-permeable body and redirects fluid advection in the hanging wall towards the distal parts of the basin, which may in turn be a contributor of the cementation growth farther into the basin (Fig. 11c). Fractures and veins within the cementation zone formed predominantly in the post-rift stage at temperatures around 30–80°C, and might reflect an extensional period during the Aptian to Turonian that has not been identified in the Wollaston Forland before. However, the fracture network did not significantly increase the permeability of the cementation zone. At continental break-up and extrusion of flood basalts in the early Eocene, the marine basin was drained allowing meteoric water to infiltrate the basin and fractures within the cemented clastics (Fig. 11d).

This study highlights the effect of rift faulting on early sediment diagenesis and shows that clastic sediments can become solidified quickly after their deposition. This has an immediate effect on the style of damage zone evolution, as it inhibits the

growth of a damage zone featuring deformation bands that would normally be expected to form in porous sediments. Instead, a fracture-dominated damage zone evolves similar to a hard-rock hosted fault. Depending on the degree of fracturing and fracture connectivity within the cementation zone, two separate, decoupled fluid circulation systems may form: one within the uncemented fault-distal sediments and one within the fractured fault zone. This may have an important impact on potential

460 mixing with fluids from under- or overlying reservoirs that are tapped by the fault.

In the management of fault-dependent subsurface aquifers/reservoirs for petroleum, groundwater or geothermal resources, and in CO_2 storage sites, it is important to be aware that in the presence of a fault-proximal cementation zone such as the one studied here, permeability and fluid flow in the vicinity of the fault may be greatly reduced. We therefore suggest, that the possibility of this type of diagenetic seal should be incorporated in fault seal analyses.

465

Data availability. Upload of replicate level raw data of the clumped isotope analysis to the EarthChem database is ongoing and a doi will be added here upon completion. In the meantime, this data can be obtained from the first author.

Author contributions. ES, AR, TBK, SAG, and GAH conducted the field data collection and rock sampling, ANM and ES operated the clumped isotope analysis, AG and RA the U-Pb analysis, and ES the optical and microprobe analyses. All authors were involved in the data
470 analysis and contributed to the manuscript writing.

Competing interests. The authors declare that they have no conflict of interest.

Acknowledgements. Arild Andresen is thanked for giving support in planning and providing equipment for the field campaign. Enver Alagoz and Sevasti Eleni Modestou are thanked for support in running the mass spectrometer for the clumped isotope analysis at University of Bergen. Muriel Erambert is thanked for support and setting up the electron microprobe data collection at University of Oslo. The Ministry
475 of Environment and Nature and the Mineral License and Safety Authority of the government of Greenland are thanked for allowing access to the Northeast Greenland National Park for fieldwork conducted under KNNO expedition permit C-18-56 and Scientific Survey License VU-00141. This study received funding from the ARCEx partners and the Research Council of Norway (grant number 228107).

References

Bellani, S., Brogi, A., Lazzarotto, A., Liotta, D., and Ranalli, G.: Heat flow, deep temperatures and extensional structures in the
480   Larderello Geothermal Field (Italy): constraints on geothermal fluid flow, Journal of Volcanology and Geothermal Research, 132, 15–
29, https://doi.org/10.1016/S0377-0273(03)00418-9, 2004.

Bernasconi, S. M., Hu, B., Wacker, U., Fiebig, J., Breitenbach, S. F. M., and Rutz, T.: Background effects on Faraday collectors in gas-
source mass spectrometry and implications for clumped isotope measurements, Rapid communications in mass spectrometry : RCM, 27,
603–612, https://doi.org/10.1002/rcm.6490, 2013.

485 Bernasconi, S. M., Müller, I. A., Bergmann, K. D., Breitenbach, S. F. M., Fernandez, A., Hodell, D. A., Jaggi, M., Meckler, A. N., Millan, I.,
and Ziegler, M.: Reducing Uncertainties in Carbonate Clumped Isotope Analysis Through Consistent Carbonate-Based Standardization,
Geochemistry, Geophysics, Geosystems, 19, 2895–2914, https://doi.org/10.1029/2017gc007385, 2018.

Brace, W. F.: Permeability of crystalline and argillaceous rocks, International Journal of Rock Mechanics and Mining Sciences & Geome-
chanics Abstracts, 17, 241–251, https://doi.org/10.1016/0148-9062(80)90807-4, 1980.

490 Chéry, J., Lucazeau, F., Daignières, M., and Vilotte, J. P.: Large uplift of rift flanks: A genetic link with lithospheric rigidity?, Earth and
Planetary Science Letters, 112, 195–211, https://doi.org/10.1016/0012-821X(92)90016-O, 1992.

Clark, I. D. and Fritz, P.: Environmental Isotopes in Hydrogeology, CRC Press, 1997.

Cooper, H., Kohout, F., Henry, H., and Glover, R.: Sea Water in Coastal Aquifers, Tech. rep., US Government Printing Office, Washington,
DC, 1964.

495 Cooper, H. H.: A hypothesis concerning the dynamic balance of fresh water and salt water in a coastal aquifer, Journal of Geophysical
Research, 64, 461–467, https://doi.org/10.1029/JZ064i004p00461, 1959.

Corti, G., van Wijk, J., Cloetingh, S., and Morley, C. K.: Tectonic inheritance and continental rift architecture: Numerical and analogue
models of the East African Rift system, Tectonics, 26, n/a–n/a, https://doi.org/10.1029/2006TC002086, 2007.

Cox, S. F.: Faulting processes at high fluid pressures: An example of fault valve behavior from the Wattle Gully Fault, Victoria, Australia,
500   Journal of Geophysical Research: Solid Earth, 100, 12 841–12 859, https://doi.org/10.1029/95JB00915, 1995.

Cumberland, S. A., Douglas, G., Grice, K., and Moreau, J. W.: Uranium mobility in organic matter-rich sediments: A review of geological
and geochemical processes, Earth-Science Reviews, 159, 160–185, https://doi.org/10.1016/j.earscirev.2016.05.010, 2016.

Dalland, A.: Mesozoic sedimentary succession at Andøy, northern Norway, and relation to structural development of the North Atlantic area,
in: Geology of the North Atlantic Borderlands, pp. 563–584, Canadian Society of Petroleum Geologists Memoir, 1981.

505 Dennis, K. J., Affek, H. P., Passey, B. H., Schrag, D. P., and Eiler, J. M.: Defining an absolute reference frame for 'clumped' isotope studies
of CO2, Geochimica et Cosmochimica Acta, 75, 7117–7131, https://doi.org/10.1016/j.gca.2011.09.025, 2011.

Ebinger, C. J., Jackson, J. A., Foster, A. N., and Hayward, N. J.: Extensional basin geometry and the elastic lithosphere, Philo-
sophical Transactions of the Royal Society of London. Series A: Mathematical, Physical and Engineering Sciences, 357, 741–765,
https://doi.org/10.1098/rsta.1999.0351, 1999.

510 Eiler, J. M.: Paleoclimate reconstruction using carbonate clumped isotope thermometry, Quaternary Science Reviews, 30, 3575–3588,
https://doi.org/10.1016/j.quascirev.2011.09.001, 2011.

Fisler, D. K. and Cygan, R. T.: Diffusion of Ca and Mg in calcite, American Mineralogist, 84, 1392–1399, https://doi.org/10.2138/am-1999-
0917, 1999.

Gawthorpe, R. L. and Leeder, M. R.: Tectono-sedimentary evolution of active extensional basins, Basin Research, 12, 195–218, https://doi.org/10.1046/j.1365-2117.2000.00121.x, 2000.

Gawthorpe, R. L., Fraser, A. J., and Collier, R. E.: Sequence stratigraphy in active extensional basins: implications for the interpretation of ancient basin-fills, Marine and Petroleum Geology, 11, 642–658, https://doi.org/10.1016/0264-8172(94)90021-3, 1994.

Gorski, C. A. and Fantle, M. S.: Stable mineral recrystallization in low temperature aqueous systems: A critical review, Geochimica et Cosmochimica Acta, 198, 439–465, https://doi.org/10.1016/j.gca.2016.11.013, 2017.

Gradstein, F. M., Ogg, J. G., Schmitz, M. D., and Ogg, G. M.: The geologic time scale 2012, Elsevier, Amsterdam and Boston, 1st ed. edn., 2012.

Harwood, J., Aplin, A. C., Fialips, C. I., Iliffe, J. E., Kozdon, R., Ushikubo, T., and Valley, J. W.: Quartz Cementation History of Sandstones Revealed By High-Resolution Sims Oxygen Isotope Analysis, Journal of Sedimentary Research, 83, 522–530, https://doi.org/10.2110/jsr.2013.29, 2013.

Henkes, G. A., Passey, B. H., Grossman, E. L., Shenton, B. J., Pérez-Huerta, A., and Yancey, T. E.: Temperature limits for preservation of primary calcite clumped isotope paleotemperatures, Geochimica et Cosmochimica Acta, 139, 362–382, https://doi.org/10.1016/j.gca.2014.04.040, 2014.

Henriksen, N.: Caledonian Orogen East Greenland 70–82 N. Geological map 1:100000, Tech. rep., GEUS, Copenhagen, Greenland, 2003.

Henstra, G. A., Grundvåg, S.-A., Johannessen, E. P., Kristensen, T. B., Midtkandal, I., Nystuen, J. P., Rotevatn, A., Surlyk, F., Sæther, T., and Windelstad, J.: Depositional processes and stratigraphic architecture within a coarse-grained rift-margin turbidite system: The Wollaston Forland Group, east Greenland, Marine and Petroleum Geology, 76, 187–209, https://doi.org/10.1016/j.marpetgeo.2016.05.018, 2016.

Henstra, G. A., Gawthorpe, R. L., Helland-Hansen, W., Ravnås, R., and Rotevatn, A.: Depositional systems in multiphase rifts: seismic case study from the Lofoten margin, Norway, Basin Research, 29, 447–469, https://doi.org/10.1111/bre.12183, 2017.

Hollinsworth, A. D., Koehn, D., Dempster, T. J., and Aanyu, K.: Structural controls on the interaction between basin fluids and a rift flank fault: Constraints from the Bwamba Fault, East African Rift, Journal of Structural Geology, 118, 236–249, https://doi.org/10.1016/j.jsg.2018.10.012, 2019.

Hollis, C., Bastesen, E., Boyce, A., Corlett, H., Gawthorpe, R., Hirani, J., Rotevatn, A., and Whitaker, F.: Fault-controlled dolomitization in a rift basin, Geology, 45, 219–222, https://doi.org/10.1130/G38s394.1, 2017.

Horita, J.: Oxygen and carbon isotope fractionation in the system dolomite–water–CO2 to elevated temperatures, Geochimica et Cosmochimica Acta, 129, 111–124, https://doi.org/10.1016/j.gca.2013.12.027, 2014.

Houben, G. J., Stoeckl, L., Mariner, K. E., and Choudhury, A. S.: The influence of heterogeneity on coastal groundwater flow - physical and numerical modeling of fringing reefs, dykes and structured conductivity fields, Advances in Water Resources, 113, 155–166, https://doi.org/10.1016/j.advwatres.2017.11.024, 2018.

Indrevær, K., Stunitz, H., and Bergh, S. G.: On Palaeozoic–Mesozoic brittle normal faults along the SW Barents Sea margin: fault processes and implications for basement permeability and margin evolution, Journal of the Geological Society, 171, 831–846, https://doi.org/10.1144/jgs2014-018, 2014.

Jiao, J. and Post, V.: Coastal hydrogeology, Cambridge University Press, Cambridge, 2019.

John, C. M. and Bowen, D.: Community software for challenging isotope analysis: First applications of 'Easotope' to clumped isotopes, Rapid communications in mass spectrometry : RCM, 30, 2285–2300, https://doi.org/10.1002/rcm.7720, 2016.

Karolytė, R., Johnson, G., Yielding, G., and Gilfillan, S. M.: Fault seal modelling – the influence of fluid properties on fault sealing capacity in hydrocarbon and CO 2 systems, Petroleum Geoscience, pp. petgeo2019–126, https://doi.org/10.1144/petgeo2019-126, 2020.

Kele, S., Breitenbach, S. F., Capezzuoli, E., Meckler, A. N., Ziegler, M., Millan, I. M., Kluge, T., Deák, J., Hanselmann, K., John, C. M., Yan, H., Liu, Z., and Bernasconi, S. M.: Temperature dependence of oxygen- and clumped isotope fractionation in carbonates: A study of travertines and tufas in the 6–95°C temperature range, Geochimica et Cosmochimica Acta, 168, 172–192, https://doi.org/10.1016/j.gca.2015.06.032, 2015.

Kim, S.-T. and O'Neil, J. R.: Equilibrium and nonequilibrium oxygen isotope effects in synthetic carbonates, Geochimica et Cosmochimica Acta, 61, 3461–3475, https://doi.org/10.1016/S0016-7037(97)00169-5, 1997.

Kristensen, T. B., Rotevatn, A., Peacock, D. C., Henstra, G. A., Midtkandal, I., and Grundvåg, S.-A.: Structure and flow properties of syn-rift border faults: The interplay between fault damage and fault-related chemical alteration (Dombjerg Fault, Wollaston Forland, NE Greenland), Journal of Structural Geology, 92, 99–115, https://doi.org/10.1016/j.jsg.2016.09.012, 2016.

Lander, R. H. and Walderhaug, O.: Predicting Porosity through Simulating Sandstone Compaction and Quartz Cementation, AAPG Bulletin, pp. 433–449, https://doi.org/10.1306/00AA9BC4-1730-11D7-8645000102C1865D, 1999.

Larsen, L. M. and Watt, W. S.: Episodic volcanism during break-up of the North Atlantic: evidence from the East Greenland plateau basalts, Earth and Planetary Science Letters, 73, 105–116, https://doi.org/10.1016/0012-821X(85)90038-X, 1985.

Larsen, L. M., Pedersen, A. K., Tegner, C., and Duncan, R. A.: Eocene to Miocene igneous activity in NE Greenland: northward younging of magmatism along the East Greenland margin, Journal of the Geological Society, 171, 539–553, https://doi.org/10.1144/jgs2013-118, 2014.

Lloyd, M. K., Ryb, U., and Eiler, J. M.: Experimental calibration of clumped isotope reordering in dolomite, Geochimica et Cosmochimica Acta, 242, 1–20, https://doi.org/10.1016/j.gca.2018.08.036, 2018.

López, D. L. and Smith, L.: Fluid flow in fault zones: Influence of hydraulic anisotropy and heterogeneity on the fluid flow and heat transfer regime, Water Resources Research, 32, 3227–3235, https://doi.org/10.1029/96WR02101, 1996.

McBride, E. F. and Milliken, K. L.: Giant calcite-cemented concretions, Dakota Formation, central Kansas, USA, Sedimentology, 53, 1161–1179, https://doi.org/10.1111/j.1365-3091.2006.00813.x, 2006.

Meckler, A. N., Ziegler, M., Millán, M. I., Breitenbach, S. F. M., and Bernasconi, S. M.: Long-term performance of the Kiel carbonate device with a new correction scheme for clumped isotope measurements, Rapid communications in mass spectrometry : RCM, 28, 1705–1715, https://doi.org/10.1002/rcm.6949, 2014.

Meinicke, N., Ho, S. L., Hannisdal, B., Nürnberg, D., Tripati, A., Schiebel, R., and Meckler, A. N.: A robust calibration of the clumped isotopes to temperature relationship for foraminifers, Geochimica et Cosmochimica Acta, 270, 160–183, https://doi.org/10.1016/j.gca.2019.11.022, 2020.

Mitchell, T. M. and Faulkner, D. R.: Towards quantifying the matrix permeability of fault damage zones in low porosity rocks, Earth and Planetary Science Letters, 339-340, 24–31, https://doi.org/10.1016/j.epsl.2012.05.014, 2012.

Mjelde, R., Breivik, A. J., Raum, T., Mittelstaedt, E., Ito, G., and Faleide, J. I.: Magmatic and tectonic evolution of the North Atlantic, Journal of the Geological Society, 165, 31–42, https://doi.org/10.1144/0016-76492007-018, 2008.

Morad, S., ed.: Carbonate cementation in sandstones: Distribution patterns and geochemical evolution, vol. 26 of *The international association of sedimentologists special publication*, Blackwell Science, [S.l.], 1998.

Morley, C. K.: Developments in the structural geology of rifts over the last decade and their impact on hydrocarbon exploration, Geological Society, London, Special Publications, 80, 1–32, https://doi.org/10.1144/GSL.SP.1995.080.01.01, 1995.

Müller, I. A., Rodriguez-Blanco, J. D., Storck, J.-C., do Nascimento, G. S., Bontognali, T. R., Vasconcelos, C., Benning, L. G., and Bernasconi, S. M.: Calibration of the oxygen and clumped isotope thermometers for (proto-)dolomite based on synthetic and natural carbonates, Chemical Geology, 525, 1–17, https://doi.org/10.1016/j.chemgeo.2019.07.014, 2019.

Passey, B. H. and Henkes, G. A.: Carbonate clumped isotope bond reordering and geospeedometry, Earth and Planetary Science Letters, 351-352, 223–236, https://doi.org/10.1016/j.epsl.2012.07.021, 2012.

Pei, Y., Paton, D. A., Knipe, R. J., and Wu, K.: A review of fault sealing behaviour and its evaluation in siliciclastic rocks, Earth-Science Reviews, 150, 121–138, https://doi.org/10.1016/j.earscirev.2015.07.011, 2015.

Phillips, T. B., Jackson, C. A.-L., Bell, R. E., Duffy, O. B., and Fossen, H.: Reactivation of intrabasement structures during rifting: A case study from offshore southern Norway, Journal of Structural Geology, 91, 54–73, https://doi.org/10.1016/j.jsg.2016.08.008, 2016.

Piasecki, A., Bernasconi, S. M., Grauel, A.-L., Hannisdal, B., Ho, S. L., Leutert, T. J., Marchitto, T. M., Meinicke, N., Tisserand, A., and Meckler, N.: Application of Clumped Isotope Thermometry to Benthic Foraminifera, Geochemistry, Geophysics, Geosystems, 20, 2082–2090, https://doi.org/10.1029/2018GC007961, 2019.

Rawling, G. C., Goodwin, L. B., and Wilson, J. L.: Internal architecture, permeability structure, and hydrologic significance of contrasting fault-zone types, Geology, 29, 43, https://doi.org/10.1130/0091-7613(2001)029<0043:IAPSAH>2.0.CO;2, 2001.

Ring, U.: The influence of preexisting structure on the evolution of the Cenozoic Malawi rift (East African rift system), Tectonics, 13, 313–326, https://doi.org/10.1029/93TC03188, 1994.

Rotevatn, A., Kristensen, T. B., Ksienzyk, A. K., Wemmer, K., Henstra, G. A., Midtkandal, I., Grundvåg, S.-A., and Andresen, A.: Structural Inheritance and Rapid Rift-Length Establishment in a Multiphase Rift: The East Greenland Rift System and its Caledonian Orogenic Ancestry, Tectonics, 37, 1858–1875, https://doi.org/10.1029/2018TC005018, 2018.

Saigal, G. C. and Bjørlykke, K.: Carbonate cements in clastic reservoir rocks from offshore Norway—relationships between isotopic composition, textural development and burial depth, Geological Society, London, Special Publications, 36, 313–324, https://doi.org/10.1144/GSL.SP.1987.036.01.22, 1987.

Salomon, E., Koehn, D., and Passchier, C.: Brittle reactivation of ductile shear zones in NW Namibia in relation to South Atlantic rifting, Tectonics, 34, 70–85, https://doi.org/10.1002/2014TC003728, 2015.

Sharp, I. R., Gawthorpe, R. L., Underhill, J. R., and Gupta, S.: Fault-propagation folding in extensional settings: Examples of structural style and synrift sedimentary response from the Suez rift, Sinai, Egypt, Geological Society of America Bulletin, 112, 1877–1899, https://doi.org/10.1130/0016-7606(2000)112<1877:FPFIES>2.0.CO;2, 2000.

Sheldon, H. A. and Micklethwaite, S.: Damage and permeability around faults: Implications for mineralization, Geology, 35, 903, https://doi.org/10.1130/G23860A.1, 2007.

Shenton, B. J., Grossman, E. L., Passey, B. H., Henkes, G. A., Becker, T. P., Laya, J. C., Perez-Huerta, A., Becker, S. P., and Lawson, M.: Clumped isotope thermometry in deeply buried sedimentary carbonates: The effects of bond reordering and recrystallization, Geological Society of America Bulletin, p. B31169.1, https://doi.org/10.1130/B31169.1, 2015.

Sheppard, S. M. F.: Characterization and isotopic variations in natural waters, Reviews in Mineralogy and Geochemistry, 16, 165–183, 1986.

Sibson, R. H.: Conditions for fault-valve behaviour, Geological Society, London, Special Publications, 54, 15–28, https://doi.org/10.1144/GSL.SP.1990.054.01.02, 1990.

Sibson, R. H., Moore, J. M. M., and Rankin, A. H.: Seismic pumping—a hydrothermal fluid transport mechanism, Journal of the Geological Society, 131, 653–659, https://doi.org/10.1144/gsjgs.131.6.0653, 1975.

625   Smeraglia, L., Berra, F., Billi, A., Boschi, C., Carminati, E., and Doglioni, C.: Origin and role of fluids involved in the seismic cycle
       of extensional faults in carbonate rocks, Earth and Planetary Science Letters, 450, 292–305, https://doi.org/10.1016/j.epsl.2016.06.042,
       2016.

Sperrevik, S., Gillespie, P. A., Fisher, Q. J., Halvorsen, T., and Knipe, R. J.: Empirical estimation of fault rock properties, in: Hydrocarbon
       seal quantification, edited by Hunsdale, R. and Koestler, A., vol. 11 of *Special publication / Norwegian Petroleum Society*, pp. 109–125,
630   Elsevier, Amsterdam [u.a.], https://doi.org/10.1016/S0928-8937(02)80010-8, 2002.

Spirakis, C. S.: The roles of organic matter in the formation of uranium deposits in sedimentary rocks, Ore Geology Reviews, 11, 53–69,
       https://doi.org/10.1016/0169-1368(95)00015-1, 1996.

Stemmerik, L., Vigran, J. O., and Piasecki, S.: Dating of late Paleozoic rifting events in the North Atlantic: New biostrati-
       graphic data from the uppermost Devonian and Carboniferous of East Greenland, Geology, 19, 218, https://doi.org/10.1130/0091-
635   7613(1991)019<0218:DOLPRE>2.3.CO;2, 1991.

Surlyk, F.: Submarine fan sedimentation along fault scarps on tilted fault blocks (Jurassic-Cretaceous boundary, East Greenland), vol. no.
       128 of *Bulletin / Grønlands Geologiske Undersøgelse*, Grønlands Geologiske Undersøgelse, Copenhagen, 1978.

Surlyk, F.: Fan-delta to submarine fan conglomerates of the Volgian-Valanginian Wollaston Foreland Group, East Greeniand., Sedimentology
       of gravels and conglomerates, in: Sedimentology of Gravels and Conglomerates, vol. 10, pp. 359–382, Canadian Society of Petroleum
640   Geology, 1984.

Surlyk, F.: Timing, style and sedimentary evolution of Late Palaeozoic-Mesozoic extensional basins of East Greenland, Geological Society,
       London, Special Publications, 55, 107–125, https://doi.org/10.1144/GSL.SP.1990.055.01.05, 1990.

Surlyk, F.: The Jurassic of East Greenland: a sedimentary record of thermal subsidence, onset and culmination of rifting, Geological Survey
       of Denmark and Greenland Bulletin, 1, 659–722, 2003.

645   Surlyk, F. and Korstgård, J.: Crestal unconformities on an exposed Jurassic tilted fault block, Wollaston Forland, East Greenland as an
       analogue for buried hydrocarbon traps, Marine and Petroleum Geology, 44, 82–95, https://doi.org/10.1016/j.marpetgeo.2013.03.009, 2013.

Surlyk, F., Hurst, J. M., Piasecki, S., Rolle, F., Scholle, P. A., Stemmerik, L., and Thomsen, E.: The Permian of the Western Margin of
       the Greenland Sea—A Future Exploration Target, in: Future Petroleum Provinces of the World, pp. 629–659, American Association of
       Petroleum Geologists, https://doi.org/10.1306/M40454C30, 1986.

650   Surlyk, F., Noe-Nygaard, N., and Dam, G.: High and low resolution sequence stratigraphy in lithological prediction—examples from
       the Mesozoic around the northern North Atlantic, Geological Society, London, Petroleum Geology Conference series, 4, 199–214,
       https://doi.org/10.1144/0040199, 1993.

Townend, J., Sutherland, R., Toy, V. G., Doan, M.-L., Célérier, B., Massiot, C., Coussens, J., Jeppson, T., Janku-Capova, L., Remaud, L.,
       Upton, P., Schmitt, D. R., Pezard, P., Williams, J., Allen, M. J., Baratin, L.-M., Barth, N., Becroft, L., Boese, C. M., Boulton, C., Broderick,
655   N., Carpenter, B., Chamberlain, C. J., Cooper, A., Coutts, A., Cox, S. C., Craw, L., Eccles, J. D., Faulkner, D., Grieve, J., Grochowski,
       J., Gulley, A., Hartog, A., Henry, G., Howarth, J., Jacobs, K., Kato, N., Keys, S., Kirilova, M., Kometani, Y., Langridge, R., Lin, W.,
       Little, T., Lukacs, A., Mallyon, D., Mariani, E., Mathewson, L., Melosh, B., Menzies, C., Moore, J., Morales, L., Mori, H., Niemeijer, A.,
       Nishikawa, O., Nitsch, O., Paris, J., Prior, D. J., Sauer, K., Savage, M. K., Schleicher, A., Shigematsu, N., Taylor-Offord, S., Teagle, D.,
       Tobin, H., Valdez, R., Weaver, K., Wiersberg, T., and Zimmer, M.: Petrophysical, Geochemical, and Hydrological Evidence for Extensive
660   Fracture-Mediated Fluid and Heat Transport in the Alpine Fault's Hanging-Wall Damage Zone, Geochemistry, Geophysics, Geosystems,
       18, 4709–4732, https://doi.org/10.1002/2017GC007202, 2017.

Vanneste, M., Guidard, S., and Mienert, J.: Bottom-simulating reflections and geothermal gradients across the western Svalbard margin, Terra Nova, 17, 510–516, https://doi.org/10.1111/j.1365-3121.2005.00643.x, 2005.

Vermeesch, P., Resentini, A., and Garzanti, E.: An R package for statistical provenance analysis, Sedimentary Geology, 336, 14–25, https://doi.org/10.1016/j.sedgeo.2016.01.009, 2016.

Walderhaug, O.: Precipitation rates for quartz cement in sandstones determined by fluid-inclusion microthermometry and temperature-history modeling, Journal of Sedimentary Research, 64, 324–333, https://doi.org/10.2110/jsr.64.324, 1994.

Wernicke, B.: Uniform-sense normal simple shear of the continental lithosphere, Canadian Journal of Earth Sciences, 22, 108–125, https://doi.org/10.1139/e85-009, 1985.

Whipp, P. S., Jackson, C. A.-L., Gawthorpe, R. L., Dreyer, T., and Quinn, D.: Normal fault array evolution above a reactivated rift fabric; a subsurface example from the northern Horda Platform, Norwegian North Sea, Basin Research, 26, 523–549, https://doi.org/10.1111/bre.12050, 2014.

Whitham, A. G., Price, S. P., Koraini, A. M., and Kelly, S. R. A.: Cretaceous (post-Valanginian) sedimentation and rift events in NE Greenland (71–77°N), Geological Society, London, Petroleum Geology Conference series, 5, 325–336, https://doi.org/10.1144/0050325, 1999.

Wibberley, C. A. and Shimamoto, T.: Internal structure and permeability of major strike-slip fault zones: the Median Tectonic Line in Mie Prefecture, Southwest Japan, Journal of Structural Geology, 25, 59–78, https://doi.org/10.1016/S0191-8141(02)00014-7, 2003.

Williams, R. T., Goodwin, L. B., Mozley, P. S., Beard, B. L., and Johnson, C. M.: Tectonic controls on fault zone flow pathways in the Rio Grande rift, New Mexico, USA, Geology, 43, 723–726, https://doi.org/10.1130/G36799.1, 2015.

Wilson, A. M.: Fresh and saline groundwater discharge to the ocean: A regional perspective, Water Resources Research, 41, 257, https://doi.org/10.1029/2004WR003399, 2005.

Worden, R. H., Morrall, G. T., Kelly, S., Mc Ardle, P., and Barshep, D. V.: A renewed look at calcite cement in marine-deltaic sandstones: the Brent Reservoir, Heather Field, northern North Sea, UK, Geological Society, London, Special Publications, 2, SP484–2018–43, https://doi.org/10.1144/SP484-2018-43, 2019.

Yielding, G., Bretan, P., and Freeman, B.: Fault seal calibration: a brief review, Geological Society, London, Special Publications, 347, 243–255, https://doi.org/10.1144/SP347.14, 2010.

Zhao, C., Hobbs, B. E., Mühlhaus, H. B., Ord, A., and Lin, G.: Convective instability of 3-D fluid-saturated geological fault zones heated from below, Geophysical Journal International, 155, 213–220, https://doi.org/10.1046/j.1365-246X.2003.02032.x, 2003.
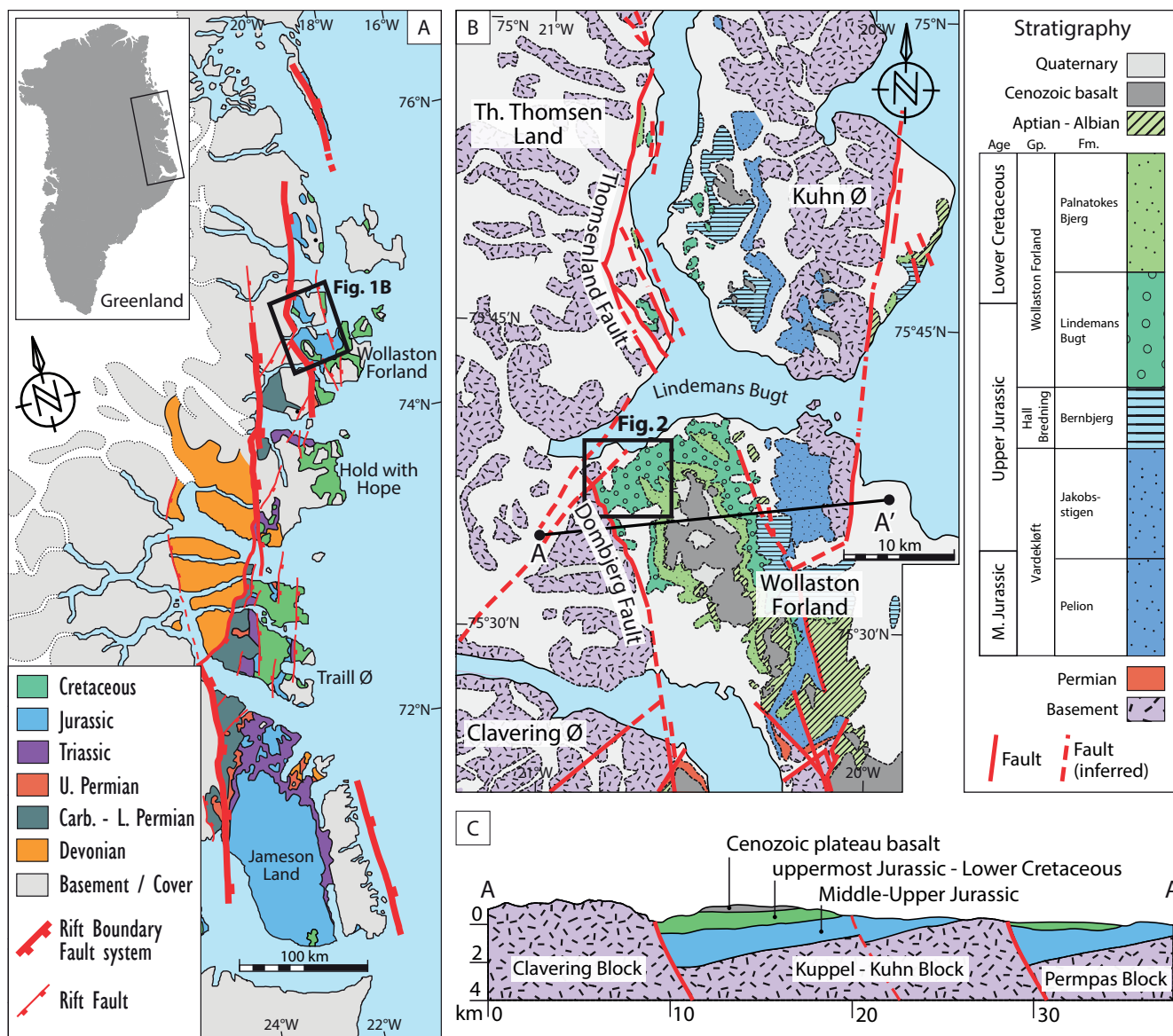
Figure 1. (a) Regional geological map of NE Greenland with right-stepping rift boundary fault system separating Devonian-Jurassic sedimentary basins from Caledonian basement. (b) Geological map of the Wollaston Forland and its surrounding. (c) Geological cross section of the Wollaston Forland Basin (see (b) for location). Modified after Rotevatn et al. (2018), based on Surlyk et al. (1993), Surlyk (2003), Henriksen (2003), Surlyk and Korstgård (2013), and Henstra et al. (2016).
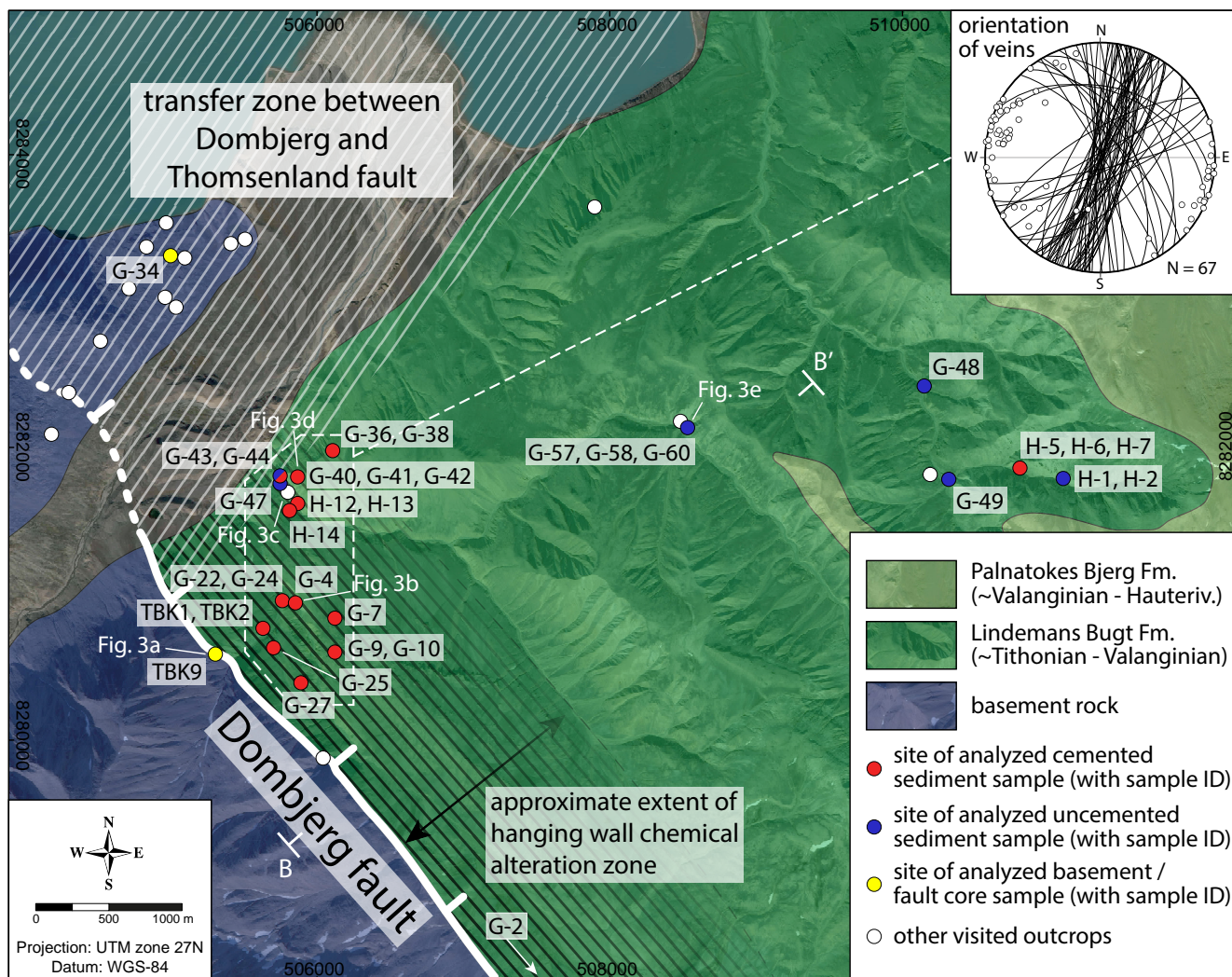
Figure 2. Geological map of study area with locations of visited outcrops and samples analyzed in this study. Inset of stereographic plot shows orientation of all collected calcite veins in the hanging wall. Profile B-B' shown in figure 9. Sample coordinates provided in supplementary table S1. See figure 1b for location. Base satellite image from © Google Maps.
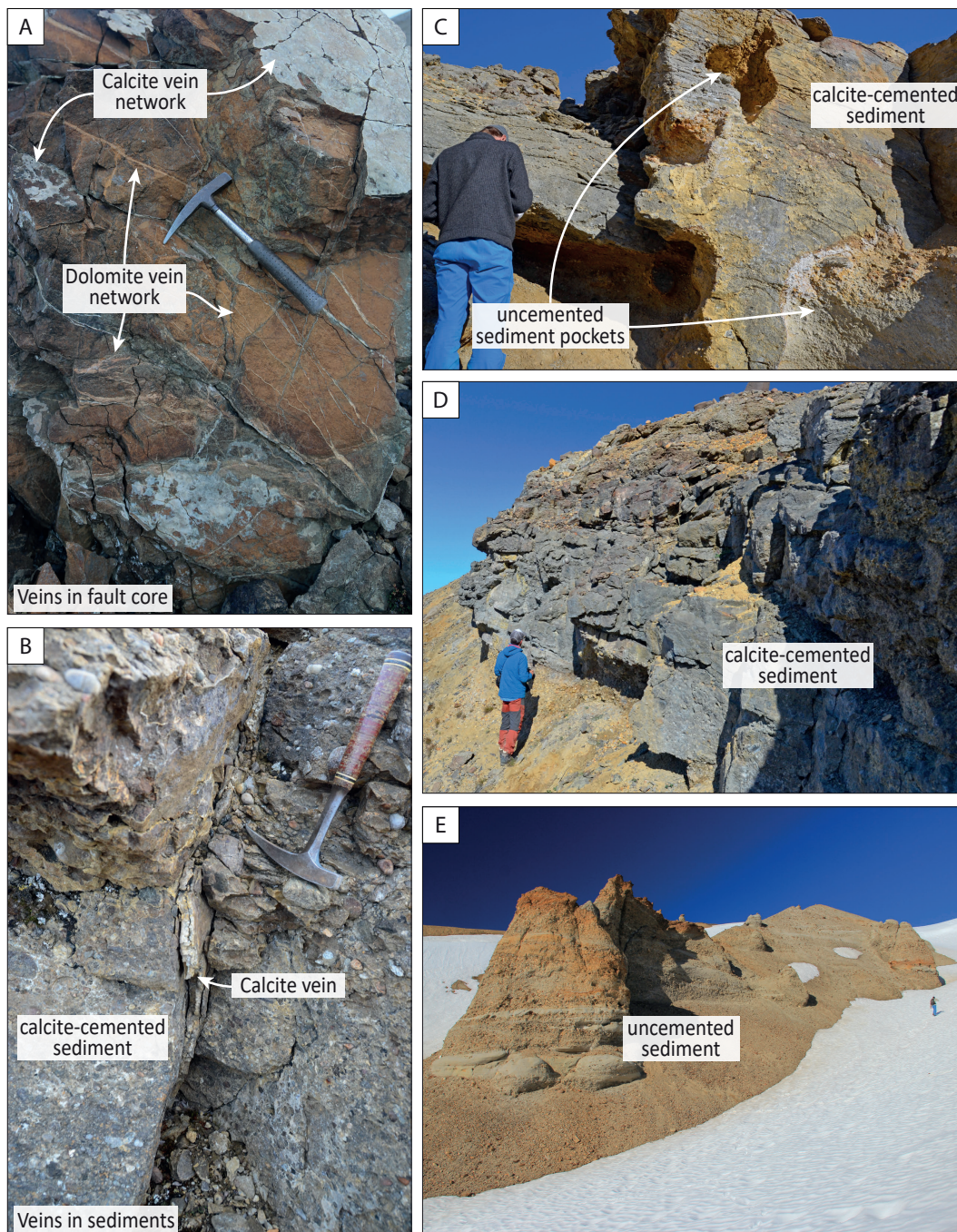
Figure 3. (a) Dolomite vein network (yellowish) cut by younger calcite vein network (whitish) in brecciated basement rock close to Dombjerg Fault core; (b) calcite vein cutting through calcite cemented sandstone within cementation zone; (c) calcite cemented sandstone with uncemented pockets at the distal end of the cementation zone; (d) calcite cemented conglomerate at distal end of the cementation zone; (e) uncemented sandstone / conglomerate outside cementation zone. For location of photos see figure 2.
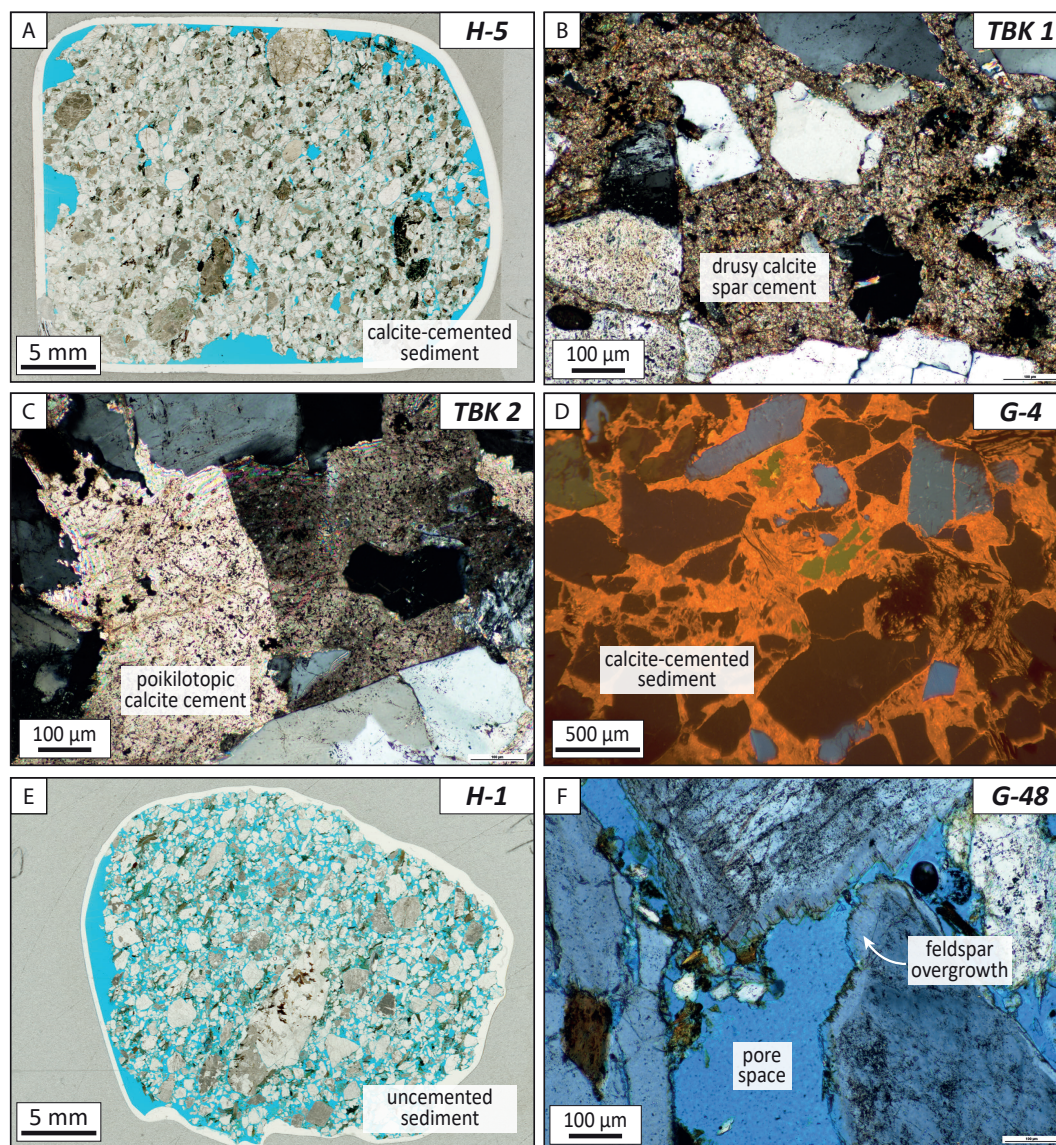
Figure 4. Thin section photos of hanging wall sediments (sample ID in respective upper right corner). (a) Calcite-cemented sample H-5 (plane-polarized light (PPL)); (b) close-up of pore-filling drusy calcite spar cement (cross-polarized light (XPL)); (c) close-up of pore-filling poikilotopic calcite cement; (d) cathodoluminescence image of calcite-cemented sample; (e) calcite-absent sediment sample H-1 (PPL); (f) close-up of calcite-absent sample with common feldspar-overgrowth (XPL with ¼ λ plate).
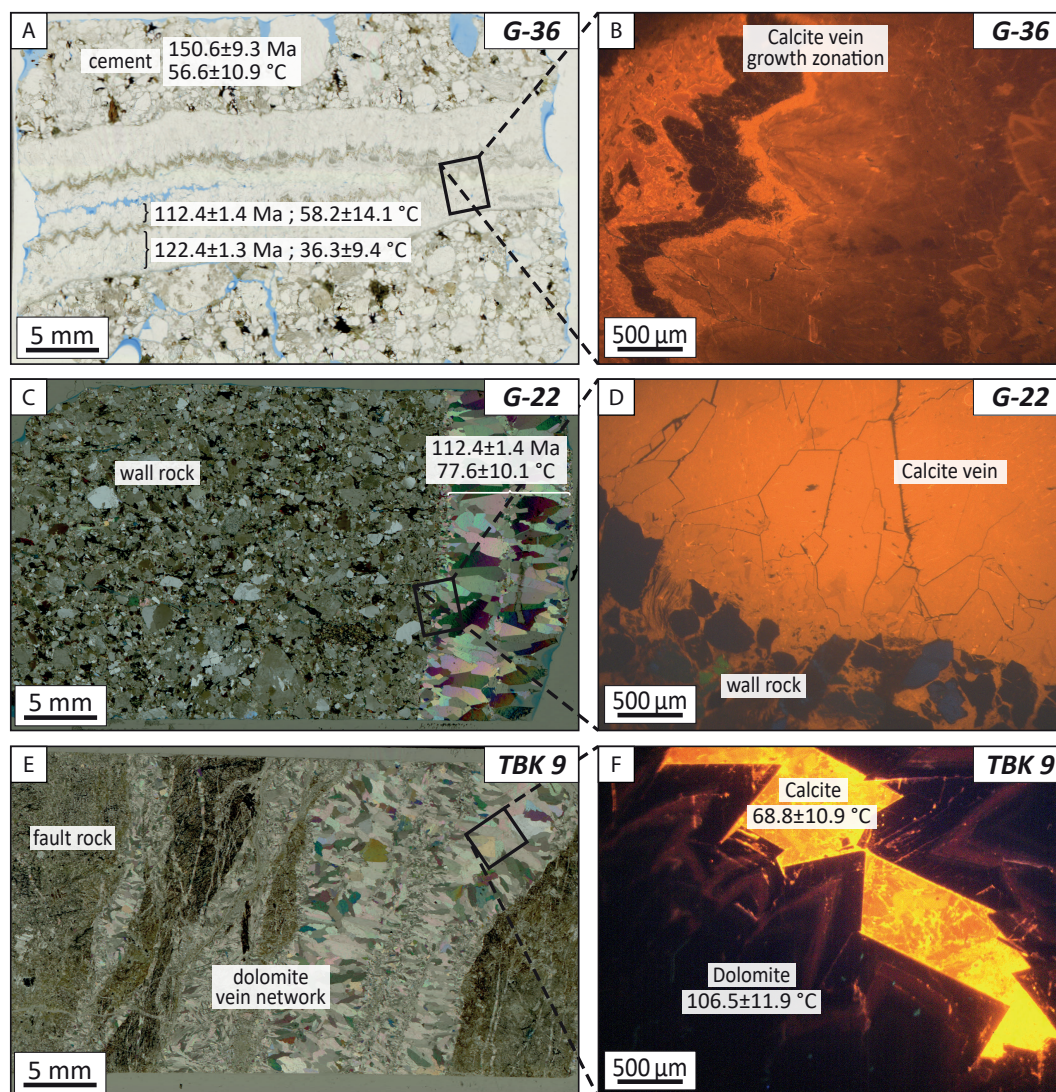
Figure 5. Thin section photos of hanging wall veins (a-d) and fault core veins (e,f). Sample ID given in upper right corner of respective image. Formation ages and temperatures given in figures where available (cf. tables 1, 2). (a) vein showing growth zonation, note ∼10 Myr age difference between outer and inner growth generation (plane-polarized light); (b) catholoduminescence (CL) close-up image of growth zonation; (c) vein devoid of growth zoning (cross-polarized light (XPL)); (d) CL close-up image of calcite vein and calcite-cemented wall rock; (e) dolomite vein network cutting through cataclasite of Dombjerg Fault core (XPL); (f) CL close-up image of dolomite crystals, remaining cavities have been filled with younger calcite.
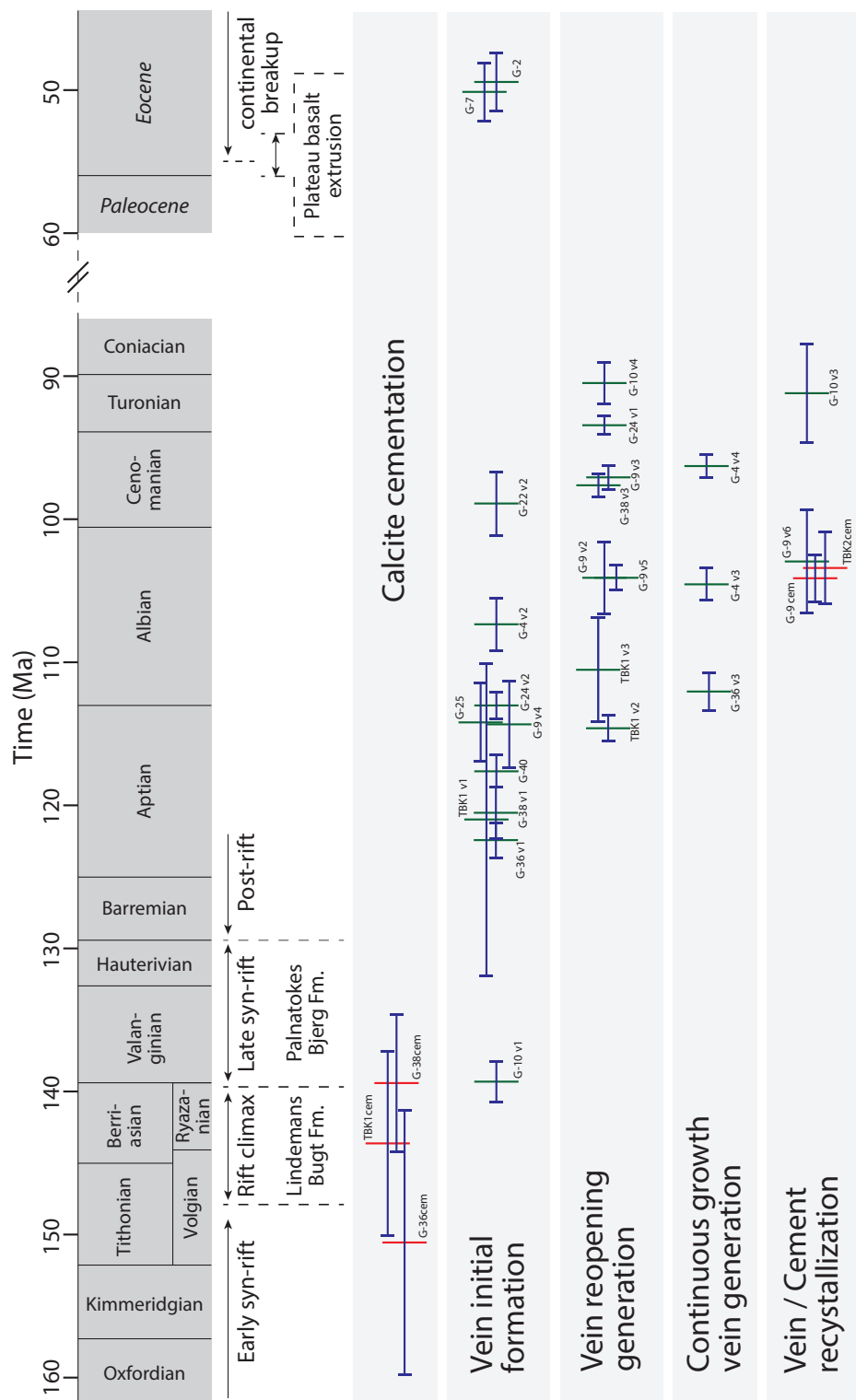
Figure 6. Timeline with formation ages of cements (red vertical bar) and veins (green vertical bar), separated into calcite cementation (cement growing in pore space), vein initial formation (first generation of calcite vein growth), vein reopening generation (calcite precipitation after renewed fracture opening of initial vein), continuous growth vein generation (veins showing continuous growth zonation after initial vein formation), and vein / cement recrystallization (ages resetted due to calcite recrystallization). All samples derive from the Lindemans Bugt Formation. Cf. table 3. Blue horizontal bars represent 2σ uncertainty. Numerical ages of regional stages Volgian and Ryazanian after Gradstein et al. (2012).
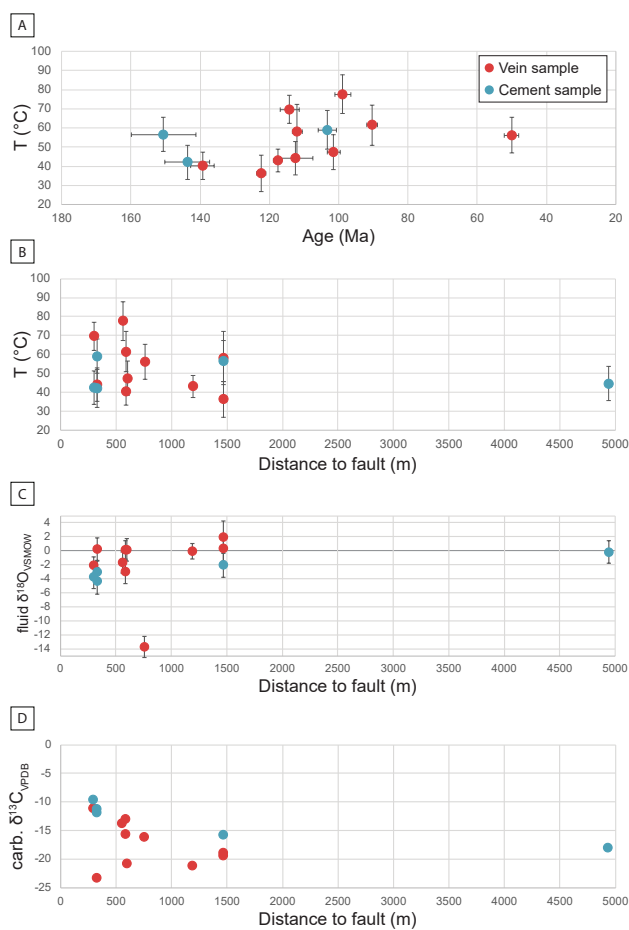
Figure 7. (a) Calcite formation temperatures obtained from clumped isotope analysis against formation ages obtained from U-Pb dating; (b) Calcite formation temperatures against distance to Dombjerg Fault; (c) Fluid $\delta^{18}O_{VSMOW}$ against distance to fault; (d) Carbonate $\delta^{13}C_{VPDB}$ against distance to fault. (error bars represent 95 % confidence interval)
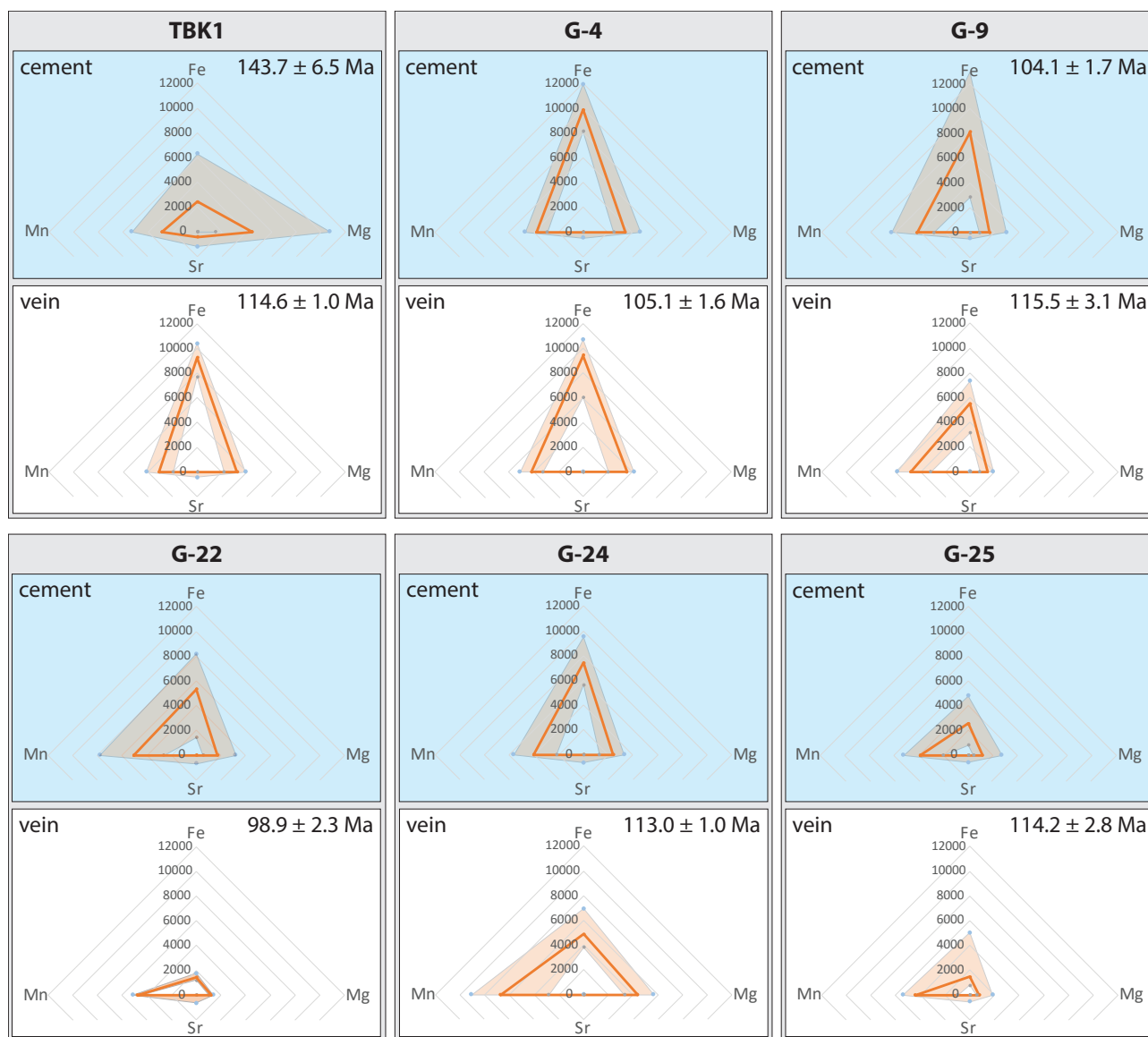
Figure 8. Diagrams showing the element concentrations of Fe, Mn, Mg, Sr in calcite cements and veins. Only samples hosting both cement and veins are shown, and among those samples with multiple vein generations, only data for the thickest vein generation is shown (see supplementary figure S2 for all diagrams). Exceptions are made for Eocene, fault core, and basement samples for which only vein data exist. Solid orange line refers to mean values, the light orange envelope to minimum and maximum values. Note the similarity of element concentration and ratio from cement to vein especially for samples G-4, G-9, G-25, and G-38. The Principal Component Analysis (PCA) plot of the mean values highlights the similar ratio (calculated using provenance R package; Vermeesch et al., 2016).
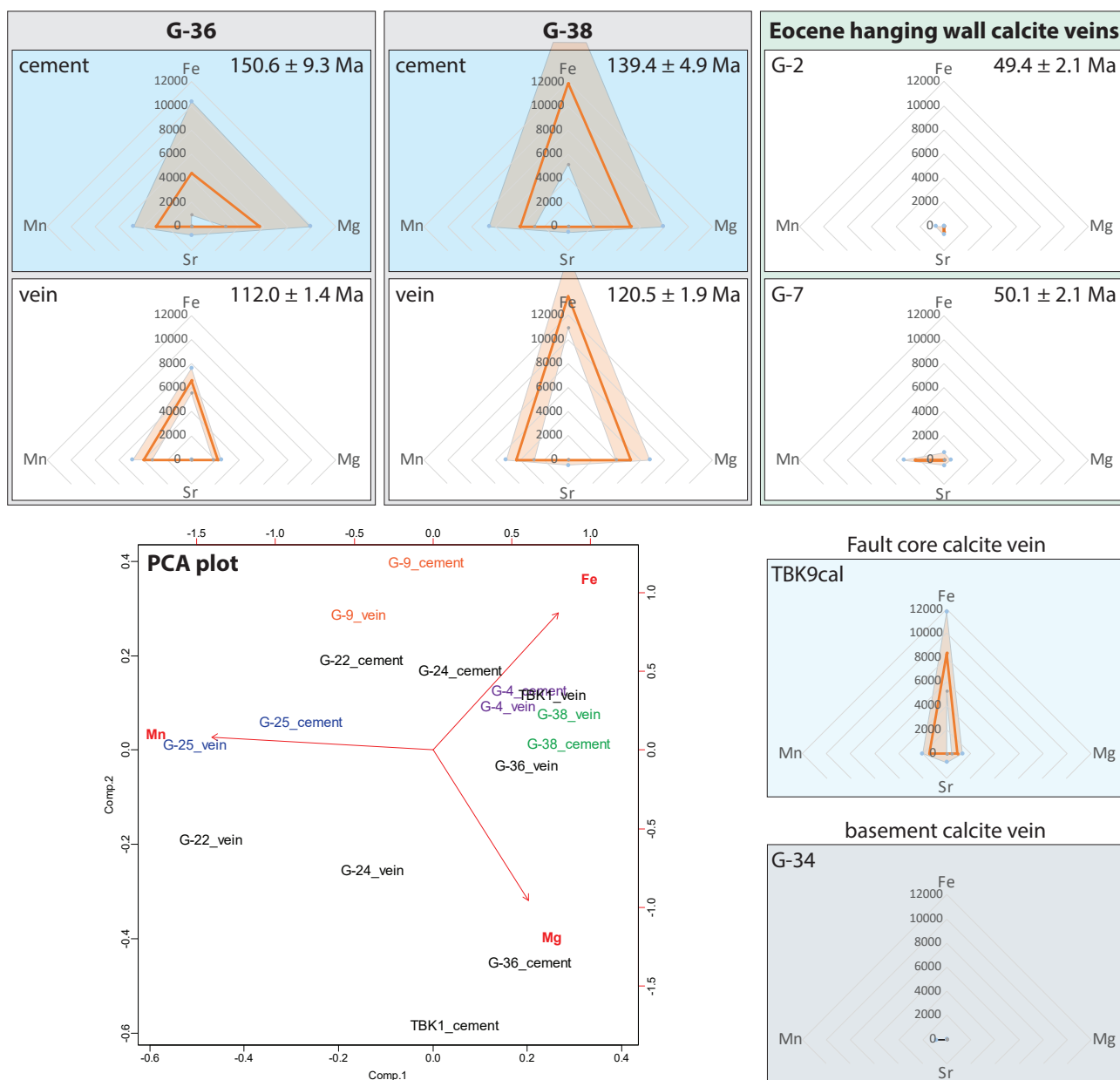
Figure 8. (continued).
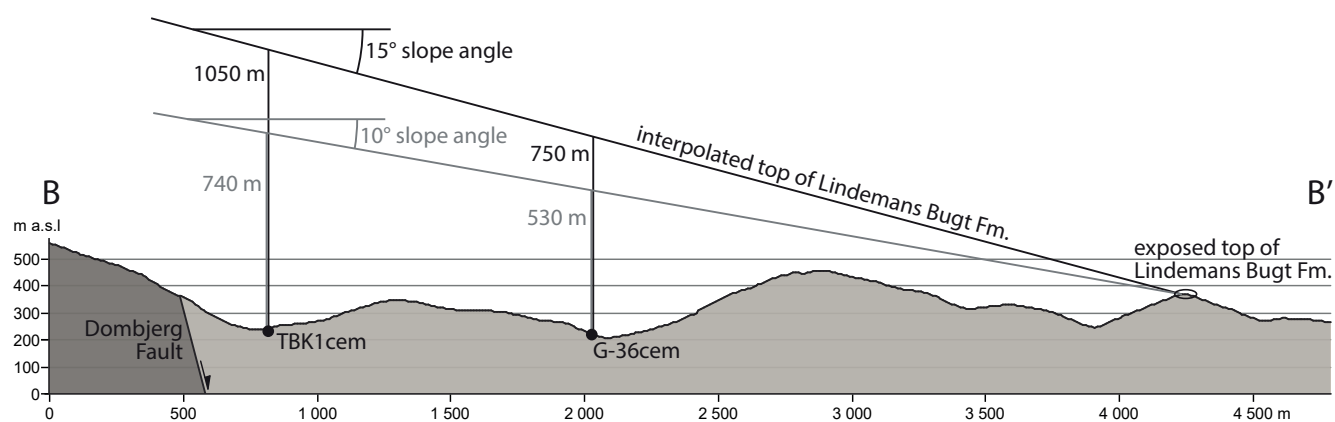
Figure 9. Estimation of thickness of Lindemans Bugt Formation above sample sites. A slope angle of 10-15° is reported for fault-proximal sediments (Henstra et al., 2016) and is used as an interpolation of the top of the formation from its exposure in the field towards the Dombjerg Fault. Sample sites are interpolated onto profile. For location of profile see figure 2.
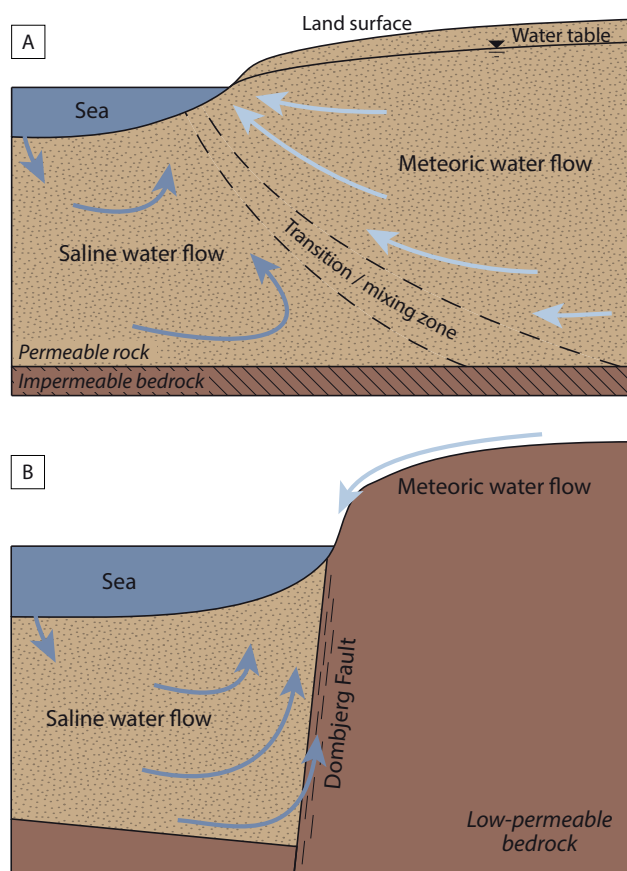
Figure 10. (a) Idealized groundwater flow in coastal areas (redrawn after Jiao and Post, 2019; Cooper et al., 1964). Circulation of saline water is tidal-, density-, and thermal-driven. (b) Conceptual adapted fluid flow model at the Dombjerg Fault in the syn-rift stage. Low-permeable footwall rock should cause dominant surficial runoff of meteoric water and circulation of saline water predominantly in the hanging wall and fault zone.
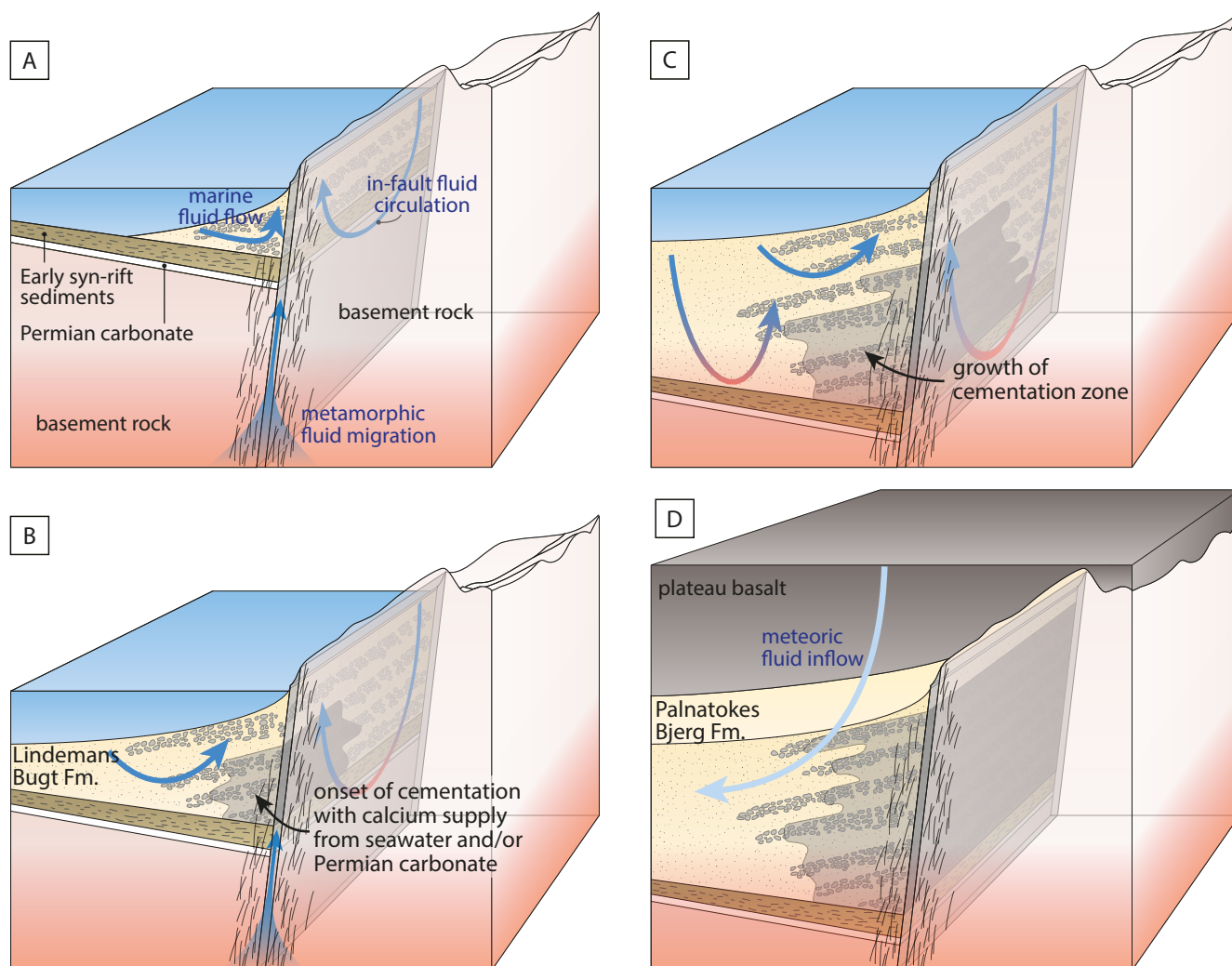
Figure 11. Schematic evolution model of fluid circulation and cementation zone along the Dombjerg Fault. (a) Onset of Dombjerg Fault activity with formation of marine hanging wall basin and syn-rift sedimentation. Circulation of marine fluids is tidal- and thermal-driven (cf. Jiao and Post, 2019). Fault activity maintains a well-connected fracture network in/near the fault core allowing for thermal-driven in-fault circulation of surficial fluids (e.g. López and Smith, 1996) and upward metamorphic fluid migration. (b) Syn-rift sedimentation continues and calcite cement starts to grow. Source of calcium is either seawater or dissolving Permian carbonate underlying syn-rift sediments. (c) Continued syn-rift sedimentation and growth of cementation zone. The zone forms a low-permeable body, which presumably directs thermal-driven marine fluid circulation farther into the basin, which may also allow the cementation zone to grow. (d) Eocene basalt extrusion and rift shoulder uplift in response to continental breakup drains the marine basin and allows meteoric fluids to intrude the hanging wall sediments.

Table 1. U-Pb calcite formation ages of calcite cements and veins of the Lindemans Bugt Formation.

Sample	Type	Age ± 2σ	MSWD
G-2	initial vein	49.4 ± 2.1	0.8
G-4 v2	initial vein	107.3 ± 1.9	0.3
G-4 v3	contin. growth vein	104.5 ± 1.2	0.7
G-4 v4	contin. growth vein	96.2 ± 0.9	1.0
G-7 v2	initial vein	50.1 ± 2.1	1.8
G-9 cem	recryst. cement	104.1 ± 1.7	2.0
G-9 v4	initial vein	114.4 ± 3.1	0.7
G-9 v2	reopening vein	104.1 ± 2.6	1.3
G-9 v3	reopening vein	97.1 ± 0.9	1.2
G-9 v5	reopening vein	104.1 ± 0.9	1.4
G-9 v6	recryst. vein	102.9 ± 3.7	2.1
G-10 v1	initial vein	139.3 ± 3.4	1.3
G-10 v3	recryst. vein	91.2 ± 3.5	1.1
G-10 v4	reopening vein	90.4 ± 1.5	1.0
G-22 v2	initial vein	98.9 ± 2.3	0.9
G-24 v2	initial vein	113.0 ± 1.0	1.4
G-24 v1	reopening vein	93.5 ± 0.7	1.0
G-25	initial vein	114.2 ± 1.8	1.8
G-36 cem	cement	150.6 ± 9.3	11.8
G-36 v1	initial vein	122.4 ± 1.3	0.8
G-36 v3	contin. growth vein	112.0 ± 1.4	0.7
G-38 cem	cement	139.4 ± 4.9	5.5
G-38 v1	initial vein	120.5 ± 1.9	0.1
G-38 v3	reopening vein	97.6 ± 0.9	0.1
G-40	initial vein	117.6 ± 1.2	1.4
TBK1 cem	cement	143.7 ± 6.5	5.8
TBK1 v1	initial vein	121.0 ± 11.0	2.0
TBK1 v2	reopening vein	114.6 ± 1.0	1.4
TBK1 v3	reopening vein	110.5 ± 3.7	1.6
TBK2 cem	recryst. cement	103.3 ± 2.6	1.8

Table 2. Results from Clumped Isotope Analysis with formation ages from U-Pb dating (cf. table 1). Uncertainties are given at the 95 % confidence interval or as uncertainty propagation (for Fluid $\delta^{18}O_{VSMOW}$), n is number of replicates measured of each sample.

type	Samples	Temp (°C)	Fluid $\delta^{18}O_{VSMOW}$	Carb. $\delta^{18}O_{VPDB}$	Carb. $\delta^{13}C_{VPDB}$	Δ_{47}	n	Age (Ma)
cements	TBK1 cem	42.0 ± 10.2	-4.3 ± 1.9	-9.7 ± 0.36	-11.3 ± 0.24	0.619 ± 0.028	14	143.7 ± 6.5
	TBK2 cem	59.0 ± 9.1	-3.0 ± 1.5	-11.3 ± 0.09	-11.9 ± 0.15	0.574 ± 0.022	14	103.3 ± 2.6
	G-25 cem	42.4 ± 8.8	-3.7 ± 1.6	-9.2 ± 0.25	-9.7 ± 0.45	0.618 ± 0.024	14	n/a
	G-36 cem	56.6 ± 10.9	-2.0 ± 1.8	-9.9 ± 0.11	-15.9 ± 0.04	0.580 ± 0.026	14	150.6 ± 9.3
	H-5	44.5 ± 9.0	-0.2 ± 1.6	-6.1 ± 0.05	-18.2 ± 0.21	0.612 ± 0.024	13	n/a
hanging wall veins	G-25	69.7 ± 7.4	-2.1 ± 1.1	-12.0 ± 0.12	-11.3 ± 0.05	0.549 ± 0.016	13	114.2 ± 2.8
	TBK1	44.1 ± 8.9	+0.2 ± 1.6	-5.6 ± 0.05	-23.5 ± 0.28	0.613 ± 0.024	14	112.5 ± 5.0
	G-10 v1	40.3 ± 7.1	+0.1 ± 1.3	-5.0 ± 0.11	-15.8 ± 0.36	0.624 ± 0.020	14	139.3 ± 3.4
	G-10 v4	61.5 ± 10.5	-3.0 ± 1.7	-11.6 ± 0.07	-13.1 ± 0.04	0.568 ± 0.024	13	90.4 ± 1.5
	G-22	77.6 ± 10.1	-1.7 ± 1.5	-12.8 ± 0.05	-13.9 ± 0.08	0.532 ± 0.020	13	98.9 ± 2.3
	G-4	47.4 ± 9.2	+0.1 ± 1.6	-6.3 ± 0.07	-20.9 ± 0.11	0.604 ± 0.024	13	101.5 ± 1.9
	G-7	55.8 ± 9.2	-13.7 ± 1.5	-21.4 ± 0.12	-16.3 ± 0.14	0.582 ± 0.022	13	50.1 ± 2.1
	G-40	43.1 ± 5.9	-0.1 ± 1.1	-5.7 ± 0.05	-21.2 ± 0.12	0.616 ± 0.016	13	117.6 ± 1.2
	G-36 v3	58.2 ± 14.1	+1.9 ± 2.3	-6.2 ± 0.05	-19.6 ± 0.08	0.576 ± 0.033	13	112.0 ± 1.4
	G-36 v1	36.3 ± 9.4	+0.3 ± 1.8	-4.1 ± 0.09	-19.0 ± 0.16	0.636 ± 0.027	13	122.4 ± 1.3
fault core vein	TBK9cal	68.8 ± 10.9	-1.8 ± 1.7	-11.7 ± 0.05	-4.2 ± 0.07	0.551 ± 0.223	13	n/a
	TBK9dol	106.5 ± 11.9	+16.2 ± 1.6	-15.3 ± 0.33	-2.2 ± 0.12	0.445 ± 0.018	13	n/a
basement vein	G-34	128.7 ± 19.1	-0.4 ± 2.1	-18.0 ± 0.04	-5.5 ± 0.04	0.445 ± 0.025	13	n/a

sorted after distance from fault core

Table 3. Minor element concentration (in ppm) of calcite cements and veins derived from microprobe analysis (bdl = below detection limit, n = number of measurements).

type	Sample ID	Fe				Mg				n
		Mean	SD	max	min	Mean	SD	max	min	
cements	G-4 cem	9902	121	11929	8138	3424	53	4637	2494	20
	G-9 cem	8116	229	12942	2833	1591	48	2949	756	20
	G-22 cem	5346	180	8187	1411	1736	79	3191	570	20
	G-24 cem	7425	104	9509	5633	2412	55	3291	1287	20
	G-25 cem	2546	107	4789	805	1152	58	2717	435	20
	G-36 cem	4392	223	10353	961	5677	172	9891	2856	20
	G-38 cem	11862	511	18854	5166	5220	178	7906	2073	20
	H-5	6255	48	7160	5532	7557	86	9553	6278	20
	TBK1 cem	2429	239	6307	*bdl*	4430	304	10727	1496	20
	TBK2 cem	3152	112	5531	1461	1309	47	2979	785	18
Hanging wall veins	G-4 v1	9399	134	10672	6026	3538	60	4124	2036	10
	G-4 v2	8827	63	9590	7432	2857	33	3462	2238	10
	G-4 v3	9356	284	12615	3035	3130	105	4351	971	10
	G-4 v4	6057	105	8396	4219	2401	31	2723	1787	20
	G-40	7323	110	9219	5260	3744	54	4485	2608	10
	G-9 v4	5492	107	7312	3145	1436	28	1902	810	10
	G-9 v5	3829	113	5853	1946	2842	87	3952	711	10
	G-10 v1	6270	219	10021	2077	1581	65	2382	330	20
	G-10 v4	2122	57	3482	1554	401	12	568	*bdl*	10
	G-22 v1	3126	100	5293	1710	1532	55	2474	851	10
	G-22 v2	1436	22	1744	1188	1204	12	1388	1017	10
	G-24 v1	9636	244	13785	6390	1754	89	3763	821	10
	G-24 v2	4888	90	6937	3826	4381	76	5686	3301	10
	G-24 v3	8245	232	11753	4511	5120	265	7140	545	10
	G-25	1472	131	5015	774	785	40	1855	552	10
	G-36 v3	6567	65	7602	5543	2207	21	2497	1814	10
	G-36 v1	8559	211	13130	5557	4269	108	6453	2753	10
	G-38 v1	13598	216	17041	10964	5180	96	6804	3981	10
	G-38 v3	12860	109	14859	11461	4766	54	5597	4038	10
	TBK1 v1	6563	141	9000	3972	3664	50	4442	2700	20
	TBK1 v2	9251	101	10381	7700	3232	61	3897	2175	10
	TBK1 v3	6635	133	8649	4048	2986	78	4303	1734	10
young veins	G-2	*bdl*	*bdl*	*bdl*	*bdl*	*bdl*	*bdl*	*bdl*	*bdl*	10
	G-7	*bdl*	*bdl*	604	*bdl*	*bdl*	*bdl*	551	*bdl*	10
basement / fault core veins	G-34	*bdl*	*bdl*	*bdl*	*bdl*	*bdl*	*bdl*	*bdl*	*bdl*	10
	TBK9dol	24556	666	33177	13823	112599	297	116761	109590	10
	TBK9cal	8342	255	11778	5235	887	33	1324	423	10

type	Sample ID	Sr				Mn				n
		Mean	SD	max	min	Mean	SD	max	min	
cements	G-4 cem	bdl	bdl	493	bdl	3741	46	4663	2882	20
	G-9 cem	bdl	bdl	523	bdl	4277	69	6310	2880	20
	G-22 cem	bdl	bdl	690	bdl	5045	113	7787	2622	20
	G-24 cem	bdl	bdl	671	bdl	4024	79	5647	2189	20
	G-25 cem	bdl	bdl	606	bdl	3895	93	5235	1988	20
	G-36 cem	bdl	bdl	737	bdl	2922	137	4806	bdl	20
	G-38 cem	bdl	bdl	502	bdl	3990	92	6550	2799	20
	H-5	bdl	bdl	554	bdl	4236	34	5039	3844	20
	TBK1 cem	421	26	1224	*bdl*	2866	137	5291	bdl	20
	TBK2 cem	bdl	bdl	639	bdl	4301	58	5172	3215	18
Hanging wall veins	G-4 v1	bdl	bdl	bdl	bdl	4153	60	5077	3253	10
	G-4 v2	bdl	bdl	508	bdl	4017	36	4468	3283	10
	G-4 v3	bdl	bdl	bdl	bdl	4227	40	5069	3733	10
	G-4 v4	bdl	bdl	846	bdl	5661	85	6256	3315	20
	G-40	bdl	bdl	bdl	bdl	3114	44	3745	2554	10
	G-9 v4	bdl	bdl	bdl	bdl	4795	67	5864	3167	10
	G-9 v5	bdl	bdl	648	bdl	3522	83	4556	1924	10
	G-10 v1	bdl	bdl	453	bdl	4125	91	5714	1979	20
	G-10 v4	bdl	bdl	666	bdl	4043	44	4727	*3334*	10
	G-22 v1	465	19	705	bdl	5103	148	7700	2720	10
	G-22 v2	bdl	bdl	651	bdl	4745	24	5130	4503	10
	G-24 v1	bdl	bdl	564	bdl	5901	205	8055	2323	10
	G-24 v2	bdl	bdl	bdl	bdl	6719	168	9044	2838	10
	G-24 v3	bdl	bdl	bdl	bdl	5694	145	8926	4106	10
	G-25	bdl	bdl	577	bdl	4387	135	5383	984	10
	G-36 v3	bdl	bdl	bdl	bdl	3959	50	4893	3279	10
	G-36 v1	bdl	bdl	444	bdl	3846	124	6303	2590	10
	G-38 v1	bdl	bdl	448	bdl	4286	89	5153	2823	10
	G-38 v3	bdl	bdl	bdl	bdl	3232	40	3974	2794	10
	TBK1 v1	bdl	bdl	503	bdl	3691	45	4519	2772	20
	TBK1 v2	bdl	bdl	429	bdl	3090	57	4120	1955	10
	TBK1 v3	bdl	bdl	464	bdl	2515	50	3152	1403	10
young veins	G-2	*472*	*14*	*706*	*bdl*	*bdl*	*bdl*	*685*	*bdl*	10
	G-7	*bdl*	*bdl*	*435*	*bdl*	2390	56	3365	*1383*	10
basement / fault core veins	G-34	*bdl*	*bdl*	*bdl*	*bdl*	*bdl*	*bdl*	*862*	*bdl*	10
	TBK9dol	2959	62	4259	2298	1219	46	1722	bdl	10
	TBK9cal	bdl	bdl	695	bdl	1435	44	2012	bdl	10